© 2019. Published by The Company of Biologists Ltd | Development (2019) 146, dev169292. doi:10.1242/dev.169292

RESEARCH ARTICLE

Syndapin constricts microvillar necks to form a united rhabdomere in *Drosophila* photoreceptors

Sakiko Ogi[1], Atsushi Matsuda[2], Yuna Otsuka[1], Ziguang Liu[1,3], Takunori Satoh[1,*] and Akiko K. Satoh[1,*]

ABSTRACT

Drosophila photoreceptors develop from polarized epithelial cells that have apical and basolateral membranes. During morphogenesis, the apical membranes subdivide into a united bundle of photosensory microvilli (rhabdomeres) and a surrounding supporting membrane (stalk). By EMS-induced mutagenesis screening, we found that the F-Bin/Amphiphysin/Rvs (F-BAR) protein syndapin is essential for apical membrane segregation. The analysis of the super-resolution microscopy, STORM and the electron microscopy suggest that syndapin localizes to the neck of the microvilli at the base of the rhabdomere. Syndapin and moesin are required to constrict the neck of the microvilli to organize the membrane architecture at the base of the rhabdomere, to exclude the stalk membrane. Simultaneous loss of syndapin along with the microvilli adhesion molecule chaoptin significantly enhanced the disruption of stalk-rhabdomere segregation. However, loss of the factors involving endocytosis do not interfere. These results indicated syndapin is most likely functioning through its membrane curvature properties, and not through endocytic processes for stalk-rhabdomere segregation. Elucidation of the mechanism of this unconventional domain formation will provide novel insights into the field of cell biology.

KEY WORDS: Syndapin, Rhabdomeres, Microvilli, F-BAR, ERM

INTRODUCTION

Epithelial cells develop two different membrane domains, apical and basolateral, that are separated by junctions. The apical surface organizes microvilli, which are membrane protrusions with actin filaments at their core. This apico-basal polarity of individual cells is required for epithelial tissue formation and function. Intensive studies have elucidated the functions of apical polarity regulators, such as Crumbs, aPKC, Cdc42, ERM proteins and PTEN, and basolateral polarity factors, such as Lgl, Dlg and Scrib, in epithelial apico-basal axis formation (Flores-Benitez and Knust, 2016; Laprise and Tepass, 2011; Rodriguez-Boulan and Macara, 2014; Tepass, 2012).

Drosophila photoreceptors differentiate from epithelial cells. During morphogenesis, the axons extend from the basolateral membrane domains and the apical plasma membranes are organized into two complementary domains: a central photosensory membrane (rhabdomere) and an adjacent supporting membrane (stalk) (Fig. 1A-C) (Karagiosis and Ready, 2004; Longley and Ready, 1995; Pichaud, 2018; Tepass and Harris, 2007). A similar segregation within the apical membrane is also observed in vertebrate photoreceptors, in which the cilia on the apical membrane differentiate into photosensitive outer segments and the remaining apical membrane is organized into inner segments. In *Drosophila*, the separation of the rhabdomere and stalk is first visible at ∼50% pupal development (pd) (Fig. 1B, red arrowheads). The rhabdomeres develop into columns of closely packed photosensitive microvilli, whereas the stalk becomes a collar of stiffened membrane that flanks the rhabdomeres and supports them on the optical axis of the eye in adult flies (Fig. 1C). Two apical polarity regulators, the Crumbs-Stardust-DPATJ (Crb-Sdt-DPATJ) complex and moesin (Moe), are involved in stalk-rhabdomere segregation (Bulgakova et al., 2008, 2010; Hong et al., 2003; Izaddoost et al., 2002; Karagiosis and Ready, 2004; Nam and Choi, 2003, 2006; Pellikka et al., 2002; Tepass, 2009, 2012). Before 50% pd, Crb and activated phosphorylated Moe (p-Moe) colocalize over the entire apical plasma membrane. However, during morphological differentiation, Crb-Sdt-DPATJ and p-Moe are partitioned into the stalk and rhabdomere base, respectively (Fig. 1D) (Karagiosis and Ready, 2004; Liu et al., 2009). In the absence of Crb-Sdt-DPATJ, the rhabdomeres expand to the stalk membrane, which is shorter than the normal stalk. However, the rhabdomeres still separate from those in the neighboring cells (Bulgakova et al., 2008, 2010; Hong et al., 2003; Nam and Choi, 2006; Pellikka et al., 2002; Pichaud, 2018; Tepass, 2012). Both Moe deficiency and dominant-active Moe expression lead to the formation of disorganized microvilli and disrupt the rhabdomere-stalk boundary (Karagiosis and Ready, 2004).

The photoreceptive rhabdomeric microvilli in *Drosophila* comprise single F-actin-cored apical plasma membrane protrusions ∼50 nm in diameter. Along each microvillus length, the membrane is attached to that of six neighboring microvilli, owing to homotypic adhesion of chaoptin (Chp) (Reinke et al., 1988). At the smooth and gently curved rhabdomere proximal face, the neighboring microvillar membranes are separate and are constricted to form the microvillus neck (Fig. 1E). Subsequently, the microvillar membranes expand and fuse to form the apical membrane floor (Fig. 1E, upper right panel). In electron micrographs of sections along the microvilli, the expanded extracellular space around the necks appears as a low electron-dense, flask-shaped white area (Fig. 1F, upper panel). In sections vertical to the microvilli, the bodies of the white flasks appear as hexagonally aligned holes representing the microvilli necks, surrounded by extracellular space (Fig. 1E,F, lower panels). Thus, the wild-type rhabdomere plasma membrane consists of two morphologically distinct membranes: (1) a floor of the apical membrane sheet, referred herein as rhabdomere base membrane; and (2) protruding photoreceptive microvilli, which are connected by thin necks. The peristyle-like structure comprising the rhabdomere base

[1]Program of Life and Environmental Science, Graduate School of Integral Science for Life, Hiroshima University, 1-7-1, Kagamiyama, Higashi-hiroshima, Hiroshima 739-8521, Japan. [2]National Institute of Information and Communications Technology, Advanced ICT Research Institute, 588-2, Iwaoka, Nishi-ku, Kobe 651-2492, Japan. [3]Institute of Animal Husbandry, Heilongjiang Academy of Agricultural Sciences, Xuefu Road No. 368, Nangang District, Harbin, Heilongjiang 150-086, China.

*Authors for correspondence: (aksatoh@hiroshima-u.ac.jp; tsatoh3@hiroshima-u.ac.jp)

Z.L., 0000-0001-9897-8653; T.S., 0000-0003-0340-5532; A.K.S., 0000-0001-7336-6642

Received 29 June 2018; Accepted 22 July 2019

Development (2019) 146, dev169292. doi:10.1242/dev.169292

membrane and microvillar necks has previously been termed the catacomb-like membrane architecture (Kumar and Ready, 1995), because the extracellular space has a catacomb-like shape.

Syndapin (also known as pacsin) is involved in several cellular processes, such as endocytosis (Kessels and Qualmann, 2004; Pérez-Otaño et al., 2006; Quan and Robinson, 2013), endocytic recycling (Gleason et al., 2016; Widagdo et al., 2016), cytokinesis (Sherlekar and Rikhy, 2016; Takeda et al., 2013), inhibition of VE-Cad internalization (Dorland et al., 2016), post-synaptic formation and function (Kumar et al., 2009b; Oh and Robinson, 2012; Schneider et al., 2014), and hair cell formation (Schüler et al., 2013). Syndapin has an F-Bin/amphiphysin/Rvs (F-BAR) domain at its N terminus. This domain forms crescent-shaped homodimers with a positively charged concave surface, which binds to negatively charged liposomes (Edeling et al., 2009; Shimada et al., 2007; Wang et al., 2009). F-BAR dimers of FBP17, CIP4 or syndapin induce the formation of 60 nm tubules *in vitro* (Edeling et al., 2009; Shimada et al., 2007; Wang et al., 2009). F-BAR domain overexpression in cultured cells induces plasma membrane invagination and tubular membrane structure formations *in vivo*. Notably, overexpression of the F-BAR domain of syndapin induces invagination as well as membrane protrusion, which has a geometry opposite to that of the tubules. In this case, syndapin localizes in the neck (Shimada et al., 2010). A model for syndapin localization in the membrane protrusion neck postulates that ∼10 syndapin molecules encircle the neck (Suetsugu and Itoh, 2012). In *Drosophila*, syndapin/CG33094 (Synd) is the sole ortholog of this protein family (Kumar et al., 2009a). Overexpression of the Synd F-BAR domain induces invaginations in S2 cells, in a manner similar to that in mammalian cells (Kumar et al., 2009b). In *Drosophila*, at the neuromuscular junctions, Synd is predominantly associated with a tubulolamellar postsynaptic membrane system known as the subsynaptic reticulum (SSR). Furthermore, overexpression of full-length Synd in the neuromuscular junctions induces SSR expansion (Kumar et al., 2009a,b).

The present study shows that Synd constricts the microvillus neck and, together with Moe, organizes the catacomb-like membrane architecture at the rhabdomere base, resulting in the segregation of the two apical membranes: stalk and rhabdomere.

RESULTS

Isolation of a mutant with an apical membrane segregation defect

Previously, screens to identify rhabdomere morphogenesis and membrane trafficking mutants (Iwanami et al., 2016; Satoh et al.,

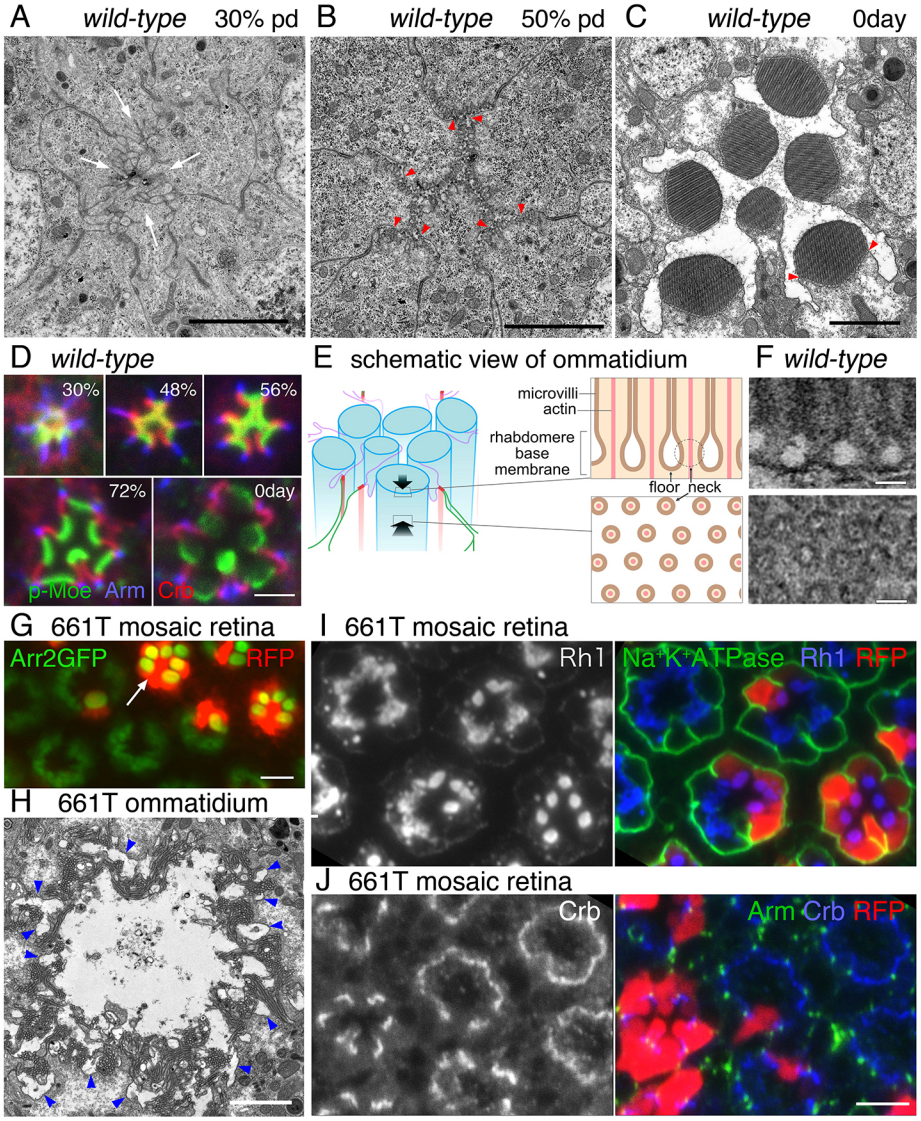

Fig. 1. Apical membrane segregation and isolation of the mutant disrupting this process. (A-C) Cross-sections of wild-type ommatidia from pupae at 30% and 50% pupal development (pd) and from adult flies observed by electron microscopy. Red arrowheads indicate the positions that separate the stalk membrane and rhabdomeres. (D) Immunostaining of wild-type ommatidia from the pupae at 30%, 48%, 56% and 72% pd, and from 0 day adult flies using anti-p-Moe (green), anti-Crb (red) and anti-Arm (blue) antibodies. (E) Schematic view of the ommatidium (left) and rhabdomere base (right). Left: adherens junctions (red), rhabdomeres (blue), stalk (violet) and basolateral membrane (green). Right: plasma membrane (brown) and F-actin (pink). (F) Electron micrographs showing high-magnification images of the rhabdomere base. (G) 661T mosaic retina from the adult fly visualized by the water-immersion technique. RFP (red) indicates wild-type cells; Arr2::GFP (green) indicates endogenous Rh1 localization in both wild-type and mutant R1-R6 peripheral photoreceptors. Arrow indicates the ommatidium composed of only the wild-type photoreceptor. (H) Cross-section of 661T homozygous ommatidium from 0 day fly observed by electron microscopy. Blue arrowheads indicate the fragmented stalk membrane. (I,J) Immunostained late pupal 661T mosaic retinas. RFP (red) indicates wild-type cells. (I) Anti-Rh1 (blue) and anti-Na^+K^+ATPase (green) antibodies. (J) Anti-Crb (blue) and anti-Arm (green) antibodies. Four independent eyes were observed in H-J. Scale bars: 2 µm in A-D,H; 50 nm in F; 5 µm in G,I,J.

Development (2019) 146, dev169292. doi:10.1242/dev.169292

2013) identified the 661T mutant allele on the right arm of chromosome 3 that resulted in rhabdomeres with a characteristic morphology (Fig. 1G). The shapes of R1-R6 peripheral photoreceptor rhabdomeres were visualized using arrestin2::GFP (Arr2::GFP), which specifically binds to photo-activated rhodopsin. In ommatidia consisting only of wild-type (RFP-positive) photoreceptors (Fig. 1G, white arrow), six round rhabdomeres clearly labeled with Arr2::GFP were separated from each other. However, in all-mutant ommatidia composed only of 661T mutant photoreceptors (Fig. 1G, RFP-negative cells), each rhabdomere was connected to its neighboring rhabdomeres at the sides, but not at the apexes. Consequently, Arr2::GFP in R1-6 photoreceptors appeared as a C-shaped figure or as a ring notched by the Arr2::GFP-negative R7 photoreceptor.

In electron microscopic analysis of the 661T mutant, the stalk membrane was not apparent and the microvilli of each photoreceptor were not united into a single round rhabdomere; however, the inter-rhabdomeric space persisted (Fig. 1H). The microvilli adhered locally to each other, even to those of neighboring photoreceptors. However, small bundles of microvilli were interrupted by small smooth membranes, presumed to comprise stalk membrane fragments (40/49 sections of mutant rhabdomere were intersected by smooth membrane. Fig. 1H, blue arrowheads). Consequently, the rhabdomeres in the mutant ommatidia formed a hollow tube, which appeared as a C-shaped figure by Arr2::GFP (Fig. 1G). The basolateral membrane, adherens junctions and cytoplasmic organelles (such as Golgi units and mitochondria) exhibited structures similar to those in the wild-type photoreceptors (Fig. S1, arrows).

Furthermore, we investigated the membrane protein localization with respect to specific plasma membrane domains in the 661T mutant photoreceptors. Consistent with our Arr2::GFP observations, the rhodopsin Rh1, which localizes to R1-R6 peripheral photoreceptor rhabdomeres, was detected across the entire apical membrane domain and appeared as a characteristic C-shaped rhabdomere in the 661T mutant photoreceptors (Fig. 1I, blue). 164/174 RFP^+ cells showed round-shaped rhabdomeres, except 10 adhering to RFP^- neighboring rhabdomere; 174/174 RFP^- cells showed irregularly shaped rhabdomeres; and 163 of them adhered to one or more neighboring rhabdomeres. The stalk membrane protein Crb was also detected across the entire apical membrane domain (Fig. 1J blue, 65/66 RFP^- cells lacked stalk-dominated Crb localization, which was maintained in 78/78 RFP^+ cells). Conversely, Na^+K^+ATPase (Fig. 1I, green, 80/82) or Arm (Fig. 1J, green, 104/104) localized to the basolateral membrane (Yasuhara et al., 2000) or adherens junctions, as in wild-type photoreceptors. These observations indicated that the apical membrane domains (stalks and rhabdomeres) were specifically affected in the 661T mutant photoreceptors.

Mutation of syndapin is responsible for the 661T mutant C-shaped rhabdomere phenotype

To identify the gene mutation responsible for the 661T mutant phenotype, we performed genetic mapping using RFLP markers (Berger et al., 2001) and found that the mutation lay between 92E8 (RFLP2392) and 93B7 (RFLP2404). Using a SOLiD next-generation sequencer, we re-sequenced the whole genome of a 661T heterozygote with the starter FRT chromosome used in the ethyl methane sulfate (EMS) screening. Only two mutations with a high impact for gene function were detected in the candidate region: (1) a missense mutation on GluRIID (GluRIID E509K) in 92F4; and (2) a nonsense mutation in syndapin (Synd Q329stop) in 93A1. To narrow down the responsible region, deficiency mapping covering 91F12 to 93B13 was performed. The heterozygotes of 661T over deletions of this region were viable, indicating a lack of lethal mutation in this 661T mutant chromosomal region. Among the heterozygous adults, only 661T over BSC43 showed C-shaped rhabdomeres by live imaging of Arr2::GFP (Fig. 2D). Other molecularly defined deletions showed normal Arr2::GFP distribution when heterozygous with 661T, indicating that the gene responsible for this phenotype is located between 3R:20,806,396 and 20,851,577, which includes syndapin, but is over 150 kb distant from GluRIID.

As the Synd nonsense mutation is a strong candidate for the 661T C-shaped rhabdomere phenotype, we performed a complementation test between the 661T chromosome and a $Synd^{mut1}$ hypomorphic allele that reduces wild-type Synd protein expression (Takeda et al., 2013). Ommatidia of 661T and $Synd^{mut1}$ hypomorphic allele trans-heterozygotes exhibited C-shaped rhabdomeres indistinguishable from those of 661T homozygous or 661T and BSC43 deficiency trans-heterozygote ommatidia (Fig. 2G). In transgenic flies (UAS-Synd) expressing full-length Synd protein under the control of Gal4,

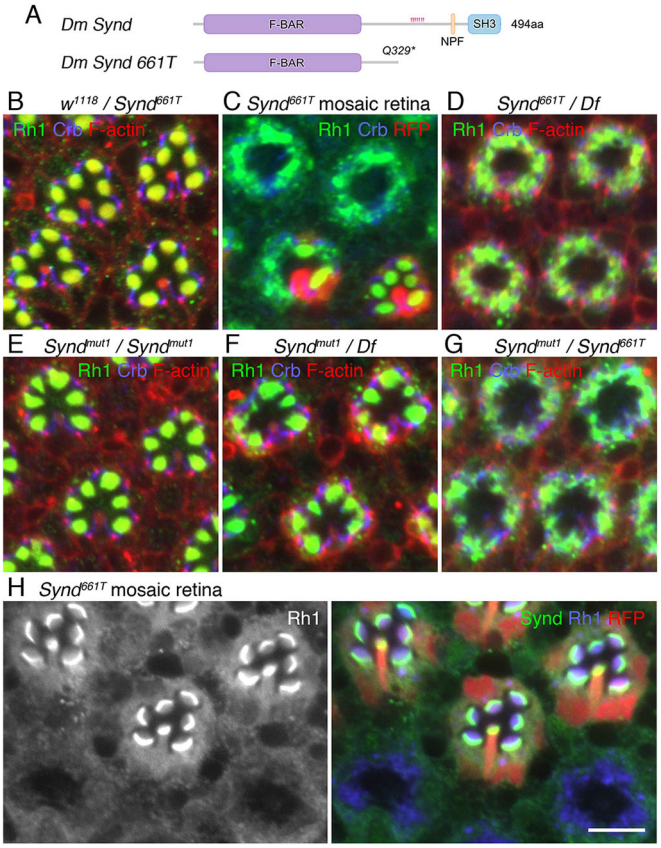

Fig. 2. *Synd^{661T}* mutation causes C-shaped rhabdomeres. (A) Schematic drawings of the protein structure of fly Synd, CG33094; upper and lower drawings represent the wild-type and 661T mutant form's structure, respectively. The fly Synd has an F-BAR domain, phosphorylation sites (red arrowheads), a NPF motif and a SH3 domain at the C terminus. (B,D-G) Immunostaining of late pupal fly retinas of the indicated genotypes using anti-Rh1 (green) and anti-Crb (blue) antibodies, and phalloidin (red). (C) Immunostaining of late pupal *Synd^{661T}* mosaic retina using anti-Rh1 (green) and anti-Crb (blue) antibodies. RFP marks the wild-type photoreceptor. (H) Immunostaining of late pupal *Synd^{661T}* mosaic retina using anti-Synd (M7) (green) and anti-Rh1 (blue) antibodies. RFP marks the wild-type photoreceptor. Five, four, three, six, three, three and two independent eyes were observed in B-H, respectively. Scale bar: 5 µm in B-H.

Development (2019) 146, dev169292. doi:10.1242/dev.169292

the Synd protein was expressed in the 661T mosaic retinas of the pupae from 20%, 50% and 70% pupal development (pd) driven by heat-shock Gal4 or Rh1 Gal4 (Fig. S2). The retinas expressing Synd from 20% pd showed normal oval-shaped rhabdomeres, confirming that the syndapin nonsense mutation caused the 661T mutant phenotype. Notably, the Synd-expressing pupal 661T photoreceptors at 50% or 70% pd showed only partial or no C-shaped rhabdomere phenotype rescue. These results indicate that a developmental window exists for proper apical membrane segregation. As we have demonstrated that the 661T mutation is a *Synd* allele, the term $Synd^{661T}$ is used hereafter.

Functional characterization of the $Synd^{661T}$ allele

The *Drosophila Synd* gene encodes a 494 amino acid polypeptide containing an F-BAR domain (amino acids 10-280) and an SH3 domain (amino acids 436-494). As the $Synd^{661T}$ allele has a nonsense mutation at 329Q, the translational $Synd^{661T}$ product lacks the SH3 but contains the F-BAR domain (Fig. 2A). We first characterized the nature of the $Synd^{661T}$ allele by genetics. Generally, null or amorphic alleles were as strong as the deletion. We compared the phenotypes of the $Synd^{661T}$ allele and *Synd* deletion in combination with either the $Synd^{661T}$ allele or $Synd^{mut1}$ hypomorphic allele. Both $Synd^{661T}$ homozygous (Fig. 2C, 180/184 RFP^- photoreceptors in mosaic retina) and $Synd^{661T}$/*Synd* deletion heterozygous ommatidia (Fig. 2D, 191/191 photoreceptors) had similar fused rhabdomeres, suggesting that $Synd^{661T}$ is a strongly hypomorphic or amorphic allele. The $Synd^{mut1}$/*Synd* deletion heterozygote ommatidia were less affected than those of the $Synd^{661T}$ homozygote or $Synd^{661T}$/*Synd* deletion heterozygote (Fig. 2F, 57/230 rhabdomere were fused), which is consistent with the hypomorphic nature of the $Synd^{mut1}$ allele.

Notably, $Synd^{mut1}/Synd^{661T}$ heterozygous ommatidia had a more pronounced C-shaped rhabdomere than the $Synd^{mut1}$/*Synd* deletion heterozygote (Fig. 2G, 174/189 rhabdomere were fused), indicating that the product of the $Synd^{661T}$ allele acts in a dominant-negative manner against the proteins expressed from the $Synd^{mut1}$ allele. However, as $Synd^{661T}$/+ heterozygous ommatidia exhibit normal rhabdomeres (Fig. 2B, 0/233 photoreceptors were fused), the dominant-negative effect of $Synd^{661T}$ protein occurs only upon low wild-type Synd expression.

We prepared antisera against peptides in the Synd protein near the N terminus (Fig. S3). All anti-Synd antisera (five derived from mice and one from rabbit) recognized a band of around 60 kDa in the head extracts of wild-type flies, which did not appear in the $Synd^{661T}$/*Synd* deletion heterozygous flies in M6, M9 and M10 immunoblots (Fig. S3A). As the predicted molecular weight of the Synd protein is 58 kDa, all the antisera recognized Synd in the blots. Furthermore, M7 and M8 produced weak bands at around 60 kDa, even in the $Synd^{661T}$/*Synd*-deletion heterozygous flies, suggesting that M7 and M8 also recognized other proteins with similar mobility. However, none of the antisera recognized a ∼38 kDa band in $Synd^{661T}$/*Synd* deletion heterozygote extracts, representing the $Synd^{661T}$ allele product predicted molecular weight (Fig. S3A). These results strongly indicate that most $Synd^{661T}$ C-terminal truncated proteins are degraded. M6 and M10 anti-Synd antisera recognized a small amount of Synd in the $Synd^{mut1}$ homozygote extracts. We determined the amount of Synd proteins in the head extracts of flies with different genotypes using the M6 anti-Synd antiserum. Consistent with the phenotype, no wild-type Synd protein was detectable in the $Synd^{mut1}/Synd^{661T}$ heterozygotes (Fig. S3C). A small amount of Synd protein was detected in the $Synd^{mut1}$/*Synd* deletion heterozygotes, suggesting that the small amount of wild-type Synd protein translated from the $Synd^{mut1}$ allele was likely degraded by the co-existence of the $Synd^{661T}$ C-terminal truncated protein. Thus, the $Synd^{661T}$ C-terminal truncated protein promotes wild-type Synd protein degradation, explaining the mechanism of its dominant-negative function. This result may suggest that the $Synd^{661T}$ product, a C-terminal truncated Synd, forms a dimer with the wild-type protein at the F-BAR domain, leading to degradation of the wild-type protein.

Synd-null phenocopies *Moe*- and *Slik*-null homozygous ommatidium

Deficiency of the sole fly ezrin/radixin/moesin (ERM) protein, Moe, or dominant-active Moe expression results in disorganized microvilli and disrupted rhabdomere/stalk boundaries in fly photoreceptors (Karagiosis and Ready, 2004). We compared the C-shaped rhabdomere phenotype of the $Synd^{661T}$ homozygous ommatidia with the Moe^{PL54}-null homozygous ommatidia rhabdomere phenotype. In the late pupal ommatidium composed of only Moe^{PL54}-null homozygous photoreceptors, both Rh1 (Fig. 3A, 0/121 RFP^+ photoreceptors, 94/94 RFP^- photoreceptors) and Crb (Fig. 3B, 0/122 RFP^+ photoreceptors, 74/75 RFP^- photoreceptors) were spread across the apical membrane domains; however, Na^+K^+ATPase (Fig. 3A, 0/121 RFP^+ photoreceptors, 1/94 RFP^- photoreceptors) and Arm (Fig. 3C, 246/246 RFP^+ photoreceptors, 195/195 RFP^- photoreceptors) localized on the basolateral membrane and adherens junctions, respectively, as in wild-type photoreceptors. The Moe^{PL54}-null homozygous ommatidium phenotype was therefore indistinguishable from that of $Synd^{661T}$ homozygotes.

Moe activity is regulated by phosphorylation (Fehon et al., 2010; McClatchey, 2014). In fly photoreceptors, p-Moe localizes at the rhabdomere base in wild-type photoreceptors (Karagiosis and Ready, 2004). The sterile 20 kinase (Slik) phosphorylates Moe (Hughes and Fehon, 2006; Hughes et al., 2010), and rhabdomere formation is adversely affected in *Slik* null mutant ($Slik^1$) photoreceptors (Hipfner et al., 2004). Thus, we investigated Slik and Moe localization in $Slik^1$ mosaic retinas. Slik and p-Moe colocalized at the rhabdomere base in the wild type; however, neither was detected in the *Slik*-deficient ommatidium (Fig. 3D, 262/262 RFP^+ photoreceptors, 0/196 RFP^- photoreceptors). These results are consistent with the previous reports showing that Slik is responsible for Moe phosphorylation at the rhabdomere base. Coincident with p-Moe loss, Rh1 (Fig. 3E, 0/123 RFP^+ photoreceptors, 186/188 RFP^- photoreceptors) and Crb spread over the apical membrane in the $Slik^1$ ommatidium (Fig. 3F, 0/135 RFP^+ photoreceptors, 171/172 RFP^- photoreceptors), whereas Na^+K^+ATPase localized normally at the basolateral membrane (Fig. 3E, 0/123 RFP^+ photoreceptors, 0/188 RFP^- photoreceptors). Electron microscopic analysis of Moe^{PL54} and $Slik^1$ homozygous ommatidia indicated that the rhabdomeric microvilli of these photoreceptors did not unite to form a single round structure, but spread to the entire apical membrane, similar to that in the $Synd^{661T}$ homozygous photoreceptors (Fig. 3G,H, 36/36 Moe^{PL54}/Moe^{PL54} and 34/34 $Slik^1/Slik^1$ photoreceptors have microvilli bundles with gap). These observations indicated that Moe phosphorylation at the rhabdomere base is essential for stalk-rhabdomere segregation.

Synd localizes at the rhabdomere base

We investigated Synd localization in the photoreceptors by immunofluorescence microscopy using the six developed anti-Synd antisera. All produced strong staining at the rhabdomere base (Fig. 2H and Fig. S3B). No staining was observed in $Synd^{661T}$

Development (2019) 146, dev169292. doi:10.1242/dev.169292

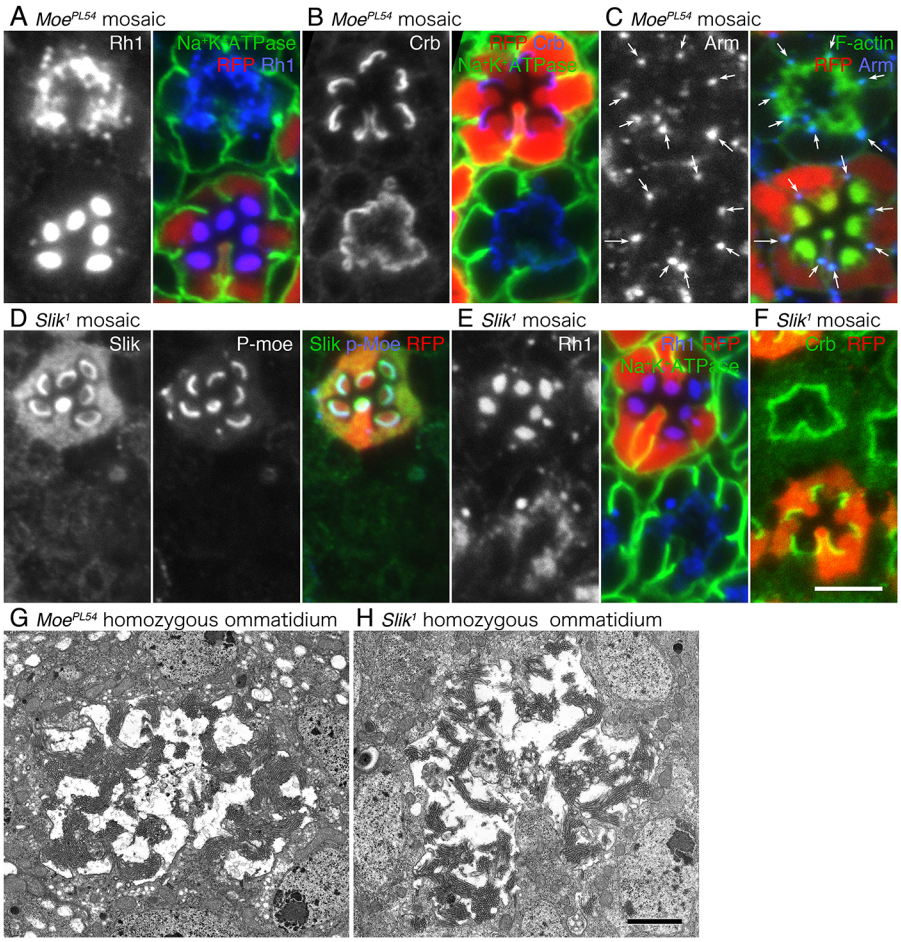

Fig. 3. Phosphorylated Moe is essential for stalk-rhabdomere segregation. (A-F) Immunostaining of *Moe*^{PL54} (A-C) or *Slik*^{1} (D-F) mosaic retinas from late pupal flies. RFP marks the wild-type photoreceptor. (A) Anti-Rh1 (blue) and anti-Na^+K^+ATPase (green) antibodies. (B) Anti-Crb (blue) and anti-Na^+K^+ATPase (green) antibodies. (C) Anti-Arm (blue) and phalloidin (green) antibodies. Adherens junctions are indicated by white arrows. (D) Anti-p-Moe (blue) and anti-Slik (green) antibodies. (E) Anti-Rh1 (blue) and anti-Na^+K^+ATPase (green) antibodies. (F) Anti-Crb antibody (green). (G,H) Cross-sections of *Moe*^{PL54} (G) and *Slik*^{1} (H) homozygous ommatidium from 0 day flies observed by electron microscopy. Three, seven, seven, seven, five, four, three and six independent eyes were observed in A-H, respectively. Scale bars: 5 µm in A-F; 2 µm in G,H.

homozygote photoreceptors, confirming that the staining represented Synd localization. These results indicate that Synd mainly localizes at the rhabdomere base.

We analyzed Synd localization during photoreceptor morphogenesis (Fig. S4A). Similar to that of p-Moe (Karagiosis and Ready, 2004), Synd colocalized with Crb on the apical membrane at 30% pd, before stalk-rhabdomere segregation. After 45% pd, Crb and Synd separated and localized on the stalk and primordial rhabdomere. Although Synd staining was observed only at the rhabdomere base at 90% pd and in adults, it is difficult to tell whether Synd localizes on only the base of the rhabdomeres or entire rhabdomeres in mid-pupal photoreceptors, because of the resolution of confocal microscopy. Synd, p-Moe and Slik colocalized on the rhabdomeres during photoreceptor morphogenesis. Higher cytoplasmic staining of Synd and Slik was observed in the pupae at 90% pd (Fig. S4B).

Synd localizes at the neck of microvilli packed into the rhabdomeres

The resolution of direct STORM (dSTORM), a type of localization microscopy, can reach 10-30 nm (Heilemann et al., 2008), which is smaller than rhabdomeric microvillar diameter. Thus, we used two-dimensional dSTORM (2D-dDTORM) to precisely localize fluorescent signals derived from anti-Synd antibodies bound to the rhabdomere base (Fig. 4A). Flies were reared in vitamin A-deficient medium to reduce rhodopsin autofluorescence. To avoid stray light from other photoreceptors, the ommatidia were isolated from the *Synd*^{661T} mosaic retina and attached to the coverslip. Synd-positive photoreceptors touching the coverslip on their basal side, without background Synd-positive photoreceptors, were chosen. Immunostaining was carried out using mouse anti-Synd and Alexa Fluor 647-conjugated secondary antibodies at concentrations higher than those used for regular immunohistochemistry to obtain nearly saturated immunofluorescence. We confirmed that these high concentrations of antibodies still produce the specific localizations of Synd and p-Moe at the base of the microvilli in the photoreceptors, and this staining disappeared in *Synd*- or *Slik*-deficient photoreceptors (Fig. S3F,G). To construct 2D-dSTORM images, movies were obtained at the level including the rhabdomere base, which was determined by anti-Synd staining. Each dye distributed to a volume of ~400 nm thickness was localized at a theoretical localization precision averaging ~10 nm in the lateral axis (Thompson et al., 2002). The 2D-dSTORM image of anti-Synd staining showed numerous foci of ~30 nm diameter (Fig. 4A). This size is roughly comparable with that of a complex of primary and secondary antibodies assembled radially around the epitopes. As both anti-Synd and anti-p-Moe photoreceptor staining are highly restricted to the rhabdomere base, these foci were considered to have originated there. Using these coordinates of the peaks, the distance to the nearest focus was measured for each focus. Most of the foci had nearest neighbors of about 50 nm distance (Fig. 4C, median±s.d.=50.2±26.0 nm, n=31,862). This distance was very similar to the distance among the rhabdomere bases previously observed with electron microscopy. In lightly stained areas of the 2D-dSTORM images, linear foci arrays spaced at about 50 nm were very often observed (Fig. 4A). In the most heavily stained regions, bright foci appeared as hexagonal arrays (Fig. 4A, rectangle) spaced

Development (2019) 146, dev169292. doi:10.1242/dev.169292

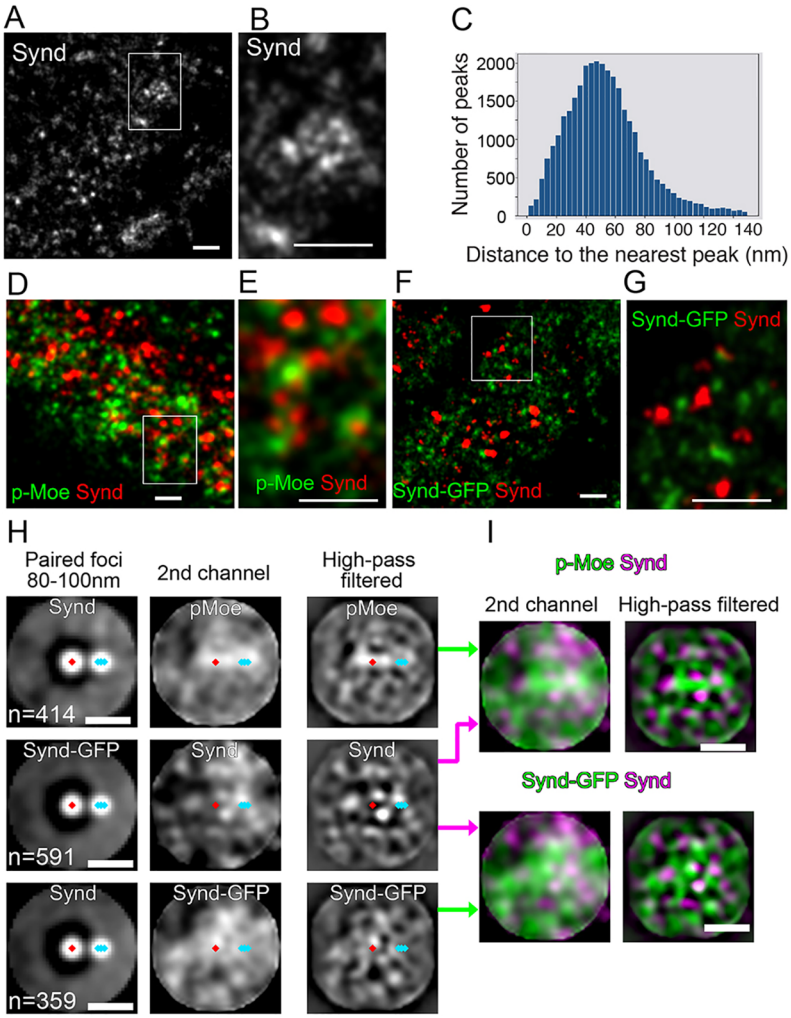

Fig. 4. Synd localization by 2D-dSTORM. Synd and p-Moe localization at the rhabdomere base in the thinner proximal region of the isolated ommatidia from late pupal flies observed from the cytoplasmic side by 2D-dSTORM. (A) Synd localization at the rhabdomere base observed by 2D-dSTORM. (B) Enlarged image (×3) of the region enclosed by the rectangle in A. (C) Plot of distances of peaks to the nearest peaks. The data are summarized from three independently imaged ommatidia. (D) Synd (red) and p-Moe (green) localization at the rhabdomere base observed by 2D-dSTORM. (E) Enlarged image (×3) of the region enclosed by the rectangle in D. (F) *Synd*^{661T} mosaic retina rescued by Synd::GFP expression induced from 20% pd was immunostained using anti-Synd (green) and anti-GFP (red) antibodies. (G) Enlarged image of the region enclosed by the rectangle in F. (H,I) Reconstruction of a fluorescent image based on the pairs of Synd foci. Paired foci detected in the Synd or Synd-GFP channel were categorized based on the distance within pairs. Images around the pairs that were 80-100 nm apart were clipped and rotated to place first foci on the center (red diamond) and second foci on the right (blue diamonds), and averaged (left and center). High-pass filtered images are also shown (right). Scale bars: 200 nm.

at ∼50 nm in such areas (Fig. 4B). Our 2D-dSTORM analysis indicated that Synd at the rhabdomere base localized in ∼50 nm-spaced arrayed spots, matching the repetitive patterns of the microvilli bundles.

To elucidate the relationship between Synd and p-Moe localization, we performed double immunolabeling of Synd and p-Moe for 2D-dSTORM analysis. Synd and p-Moe exhibited localization patterns with least overlaps (Fig. 4D). In heavily stained regions, wherein the bright Synd foci appeared as hexagonal arrays, the p-Moe signals localized between the Synd foci (Fig. 4E), which is distinct from control two-color dSTORM images of Synd and Synd-GFP (Fig. 4F,G). To evaluate the regularity of Synd foci, we performed unbiased reconstruction of two-color dSTORM images around detected Synd foci. From two-color dSTORM images of Synd/p-Moe and Synd/Synd-GFP, detected Synd foci were paired with the nearest neighbor and categorized by the distance within each pair. The images around the pairs were rotated to locate the first focus to the center and the second focus to the right, and averaged to reconstruct two-color images around the Synd foci pairs in distance of certain range (Fig. 4H,I). If Synd exists in a repetitive pattern, the second channel is expected to represent the distribution of fluorescence relative to the repetitive pattern of Synd. In the reconstruction based on 80-100 nm Synd-GFP pairs, Synd showed a hexagonal array of spots ∼50 nm apart, as expected. The pattern of p-Moe reconstructed based on Synd was less clear, but showed some tendency to avoid Synd when compared with Syd/Synd-GFP. These results imply that Synd but not p-Moe localizes to the neck of the microvilli.

As the 2D-dSTORM analysis showed that Synd localized in 50-nm hexagonally arrayed spots, the microstructure of the rhabdomere base was reinvestigated (Fig. 5A). Assuming the structural symmetry of the rhabdomere base membrane, no structures other than microvillar necks matched the 50 nm hexagonal array. In the electron micrographs of sections along the microvilli longitudinal axis, the narrowest part of the microvillar necks appeared to be ∼25 nm in diameter, which is about half the distance between neighboring microvilli centers. Neck longitudinal curvature was about 20 nm in radius (Fig. 5B,C). A model of syndapin at the protrusion (Suetsugu and Itoh, 2012) suggests that the concave side of the syndapin dimer curves the membrane at the protrusion base. Crystal structure analysis indicated that the radius of curvature of the membrane bounded by *Drosophila* Synd is 21 nm (Edeling et al., 2009).

In the cross-section of the rhabdomere base, microvillar necks were found in the area between the microvilli and cytoplasm (Fig. 5A). As the neck height is similar to the section thickness, only longitudinal projections of the microvillar neck can be obtained (Fig. 5C). However, the detailed structures are still visible, and the approximate level of the section depth can be estimated by the histological context and the size of the extracellular space surrounding the neck (Fig. 5D). Actin filaments were present at the center of most microvillar necks. Between the cytoplasm and

Development (2019) 146, dev169292. doi:10.1242/dev.169292

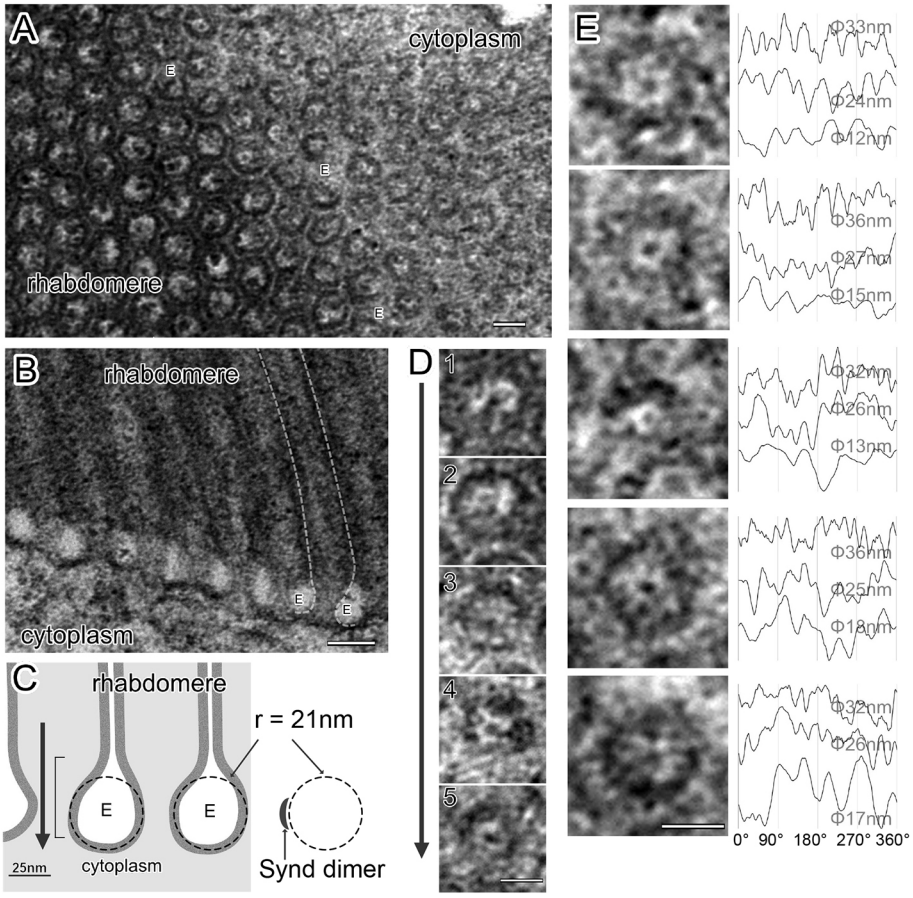

Fig. 5. Structural detail of the microvillar necks by electron microscopy. (A) Electron micrograph of a section vertical to the photoreceptor microvilli of a 0 day adult fly at the level of the microvillar necks. 'E' indicates extracellular spaces. (B) Section of microvillar neck along the longitudinal axis of the microvilli. The pear-shaped extracellular spaces around the necks are indicated by 'E'. (C) Left: schematic drawing of a microvillar neck along the microvillus longitudinal axis. Black bracket represents 80 nm, the typical section thickness. Right: dimension of F-BAR-domain dimer of fly Synd based on crystal structure (Edeling et al., 2009). (D) Sections of the microvillar necks at various estimated levels. The approximate levels of the sections are shown by an arrow in C. (E) Gallery of sections of the microvillar necks with ring arrays of electron-dense spots. Intensities are plotted along the concentric circles for the radiuses showing peaks. For each image, three plots by radius showing highest peak and valley waves were chosen for display. Scales of the profile are normalized and offset along the *y*-axis. Scale bars: 50 nm in A; 25 nm in B-E.

extracellular space, ring arrays of electron-dense spots were often visible (Fig. 5D, panels 3-5) but not seen in sections above the microvillar neck (Fig. 5D, panel 1). The circular intensity profile plots along the radii from the center of the microvilli indicated that the spots were aligned on ring arrays. Most of the inner ring arrays were 12-18 nm in diameter and typically six dense spots (Fig. 5E). The microvillar neck size appeared sufficient to house five or more Synd dimers along the internal surface. Considering the 2D-dSTORM analysis results, our observations indicate that the Synd protein likely localizes at each microvillus neck. Additionally, outer ring arrays containing 10-15 dense spots were observed at 24-36 nm from the center (Fig. 5D,E), which correspond to the mossy electron-dense structures underneath the bottom of pear-shaped extracellular spaces observed in the vertical sections (Fig. 5B).

Catacomb-like membrane architecture is lost in *Synd*^{661T}, *Moe*^{PL54} and *Slik*^{1} homozygous photoreceptors

As Synd, p-Moe and Slik localize at the rhabdomere base (Figs 2H and 3D), we performed an electron microscopic investigation of the structures at the microvillus base in the *Synd*^{661T}, *Moe*^{PL54} and *Slik*^{1} homozygote photoreceptors at day 0 of adulthood. The microvilli necks and the rhabdomere base membrane constituting the catacombs were completely lost, and the microvilli protruded from the apical membrane without any curved membrane (Fig. 6B-D, 24/24 *Synd*^{661T}/*Synd*^{661T}, 34/34 *Slik*^{1}/*Slik*^{1}, 35/35 *Moe*^{PL54}/*Moe*^{PL54} photoreceptors). Thus, Synd, p-Moe and Slik are required for formation of the catacomb-like membrane architecture.

As the catacombs develop during late pupal morphogenesis (Kumar and Ready, 1995), we investigated the pupal microvillar and neck structures in wild-type and *Synd*^{661T}/*Synd* deletion heterozygous photoreceptors at 60%, 74% and 90% pd (Fig. 6E-H). Although the catacombs were not well developed in the wild-type photoreceptors at 60% and 74% pd, there was still a curved membrane at the microvillus base (Fig. 6F, arrows). At these developmental stages, in the *Synd*^{661T}/*Synd* deletion heterozygous photoreceptors, the effect on microvillus unity was mild: the microvilli were not tightly packed but clear stalk membranes were observed between the adherens junction and rhabdomeres (Fig. 6G). The curved membrane at the microvillus base in the wild-type photoreceptors was not observed in the *Synd*^{661T} homozygous photoreceptors (Fig. 6F,H). At 90% pd, the catacomb-like membrane architecture was already well organized in the wild type, whereas the stalk-rhabdomere segregation was severely disrupted in the *Synd*^{661T}/*Synd* deletion heterozygous photoreceptors (Fig. 6G). Thus, mutant phenotype development in the *Synd*^{661T}/*Synd* deletion heterozygous photoreceptors partly corresponded to the stage for catacomb-like structure formation.

Moe and Synd are independently recruited to the rhabdomere base and function in the same process for apical membrane separation

To elucidate the relationship between Synd and Moe function, we investigated the mutual dependence for their recruitment to the rhabdomere base. The Synd protein localized on the *Moe*^{PL54} homozygous photoreceptor apical membrane (Fig. 7A, 215/216 *Moe*^{PL54}/*Moe*^{PL54} photoreceptors) and p-Moe localized on that of the *Synd*^{661T} homozygous photoreceptor (Fig. 7B, 198/199 *Synd*^{661T}/*Synd*^{661T} photoreceptors). Thus, Synd and p-Moe are independently recruited to the rhabdomere base, even in the absence of catacombs.

Development (2019) 146, dev169292. doi:10.1242/dev.169292

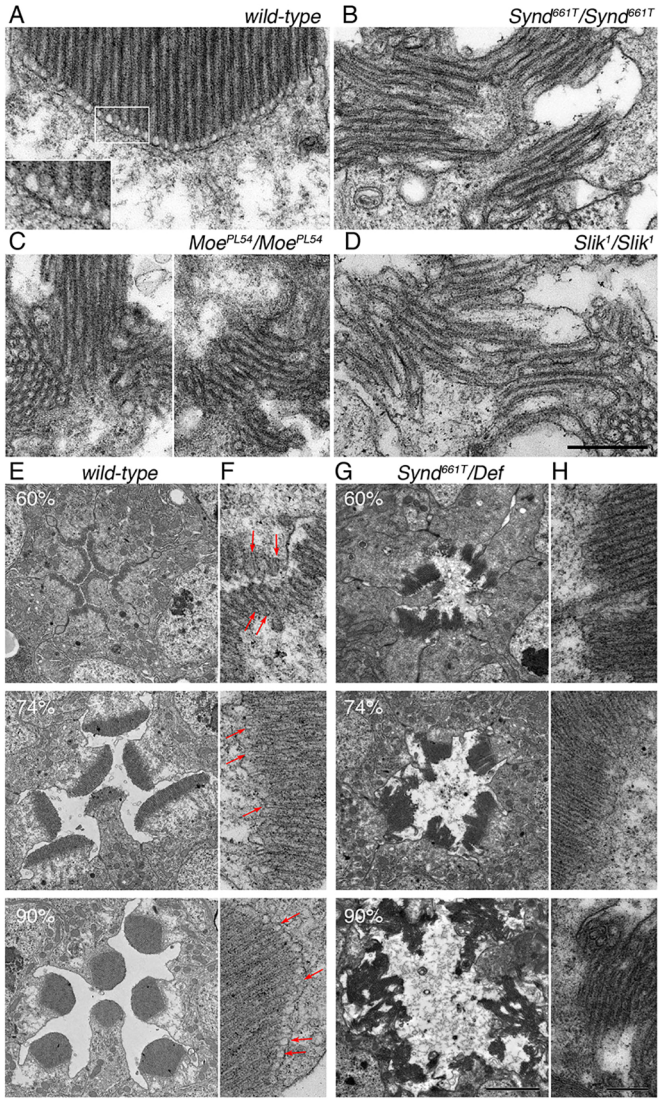

Fig. 6. Synd is required for catacomb-like membrane architecture formation. (A-D) Magnified cross-sections at the rhabdomere base of wild-type (A), *Synd*^{661T} (B), *Moe*^{PL54} (C) and *Slik*^{1} (D) homozygous 0 day flies observed by electron microscopy. (E-H) Cross-sections of the ommatidia and rhabdomere base of wild-type (E,F) and *Synd*^{661T}/Def (G,H) pupae at 60%, 74% and 90% pd observed by electron microscopy. Arrows indicate the curved membranes. Seven, seven, six and three independent eyes were observed in A-D, respectively. Scale bars: 500 nm in A-D,F,H; 2 µm in E,G.

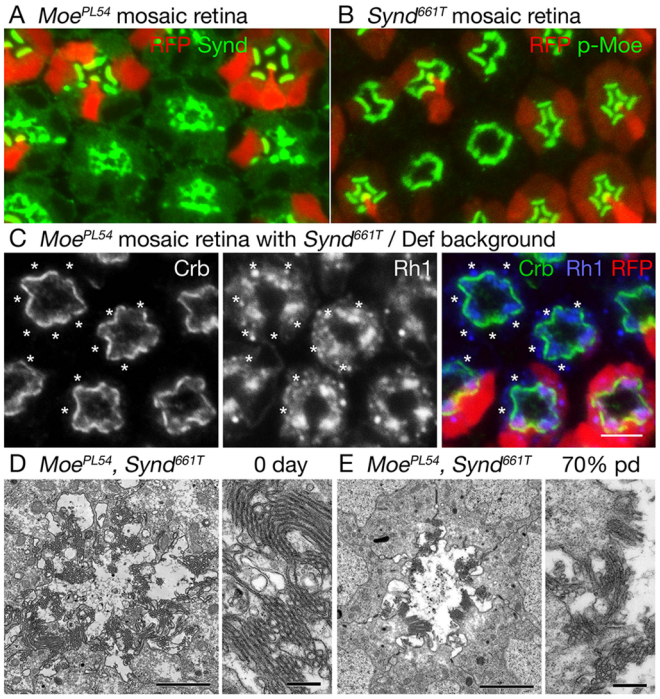

Fig. 7. Loss of Moe does not enhance the disruption of stalk-rhabdomere segregation caused by Synd deficiency. (A) Immunostaining of late pupal *Moe*^{PL54} mosaic retinas using anti-Synd (green) antibodies. RFP marks the wild-type photoreceptor. (B) Immunostaining of late pupal *Synd*^{661T} mosaic retinas using anti-p-Moe (green) antibodies. RFP marks the wild-type photoreceptor. (C) Immunostaining of late pupal *Moe*^{PL54} mosaic retinas using *Synd*^{661T}/Def background with anti-Crb (green) and anti-Rh1 (blue) antibodies. RFP marks the *Synd* single-mutant photoreceptor. Asterisks show *Synd* and *Moe* double-mutant photoreceptors. (D,E) Cross-sections of an ommatidium of *Moe*^{PL54} homozygous photoreceptors with *Synd*^{661T}/Def background in 0 day adult flies (D) and the pupae at 70% pd (E) observed by electron microscopy. Five, twelve, three, two and three independent eyes were observed in A-E, respectively. Scale bars: 5 µm in A-C; 2 µm in D,E, left; 500 nm in D,E, right.

Furthermore, we investigated the phenotype of the *Moe*^{PL54} and *Synd*^{661T} double-mutant ommatidium and compared it with that of the *Synd*^{661T} single mutant by generating a *Moe*^{PL54} mosaic retina on a *Synd*^{661T}/*Synd* deletion heterozygous background. Notably, extent of stalk-rhabdomere segregation defect did not differ between the double homozygous mutant of *Moe*^{PL54} and *Synd*^{661T}, and *Synd*^{661T} single homozygous mutant based on stalk membrane marker Crb and rhabdomere protein Rh1 immunostaining (Fig. 7C, 136/136 single- and 95/95 double-mutant photoreceptors) or by electron microscopic analysis (Figs 1H and 7D, 24/24 double-mutant photoreceptors). During the development of both *Moe*^{PL54}, *Synd*^{661T} double-mutant and *Synd*^{661T} single-mutant ommatidia, Crb and TRP staining were partially separate (Fig. S5A,D), and largely intact stalk membranes existed adjacent to the adherens junctions in electron micrographs (Fig. 7E, 46/48 double-mutant photoreceptors), indicating that the stalk-rhabdomere segregation defects appear during catacomb-like membrane architecture formation. These results strongly indicate that Moe and Synd are recruited in a mutually independent manner, and that the lack of one disrupts the other's function. Thus, Synd and p-Moe must function in the same/close process for stalk-rhabdomere segregation.

Chp and Synd independently regulate stalk-rhabdomere segregation

The GPI-anchored protein Chp was originally identified as an adherens molecule between the microvilli within a rhabdomere (Reinke et al., 1988). Additionally, Crb mislocalizes on the rhabdomere in addition to the stalk membrane in *chp*^{2} null photoreceptors, indicating that Chp might be required, either directly or indirectly, for apical membrane segregation into the rhabdomere and stalk (Gurudev et al., 2014). Our result reproduced Crb mislocalization on the rhabdomeres in the *chp*^{2} null photoreceptors (Fig. S5C,C′, arrows). However, we also found that TRP specifically localized to the rhabdomeres and Synd localized normally at the rhabdomere base without accumulation on the stalk (Fig. 8A, 102/102 *chp*^{2}/*chp*^{2} photoreceptors). Furthermore, in electron microscopy, the stalk and rhabdomeres are separated perfectly in the *chp*^{2} homozygous photoreceptors. Correspondingly, the microvillar necks were well developed in the *chp*^{2} null photoreceptors (Fig. 8C, lower magnified image, 35/35 *chp*^{2}/*chp*^{2} photoreceptors).

Development (2019) 146, dev169292. doi:10.1242/dev.169292

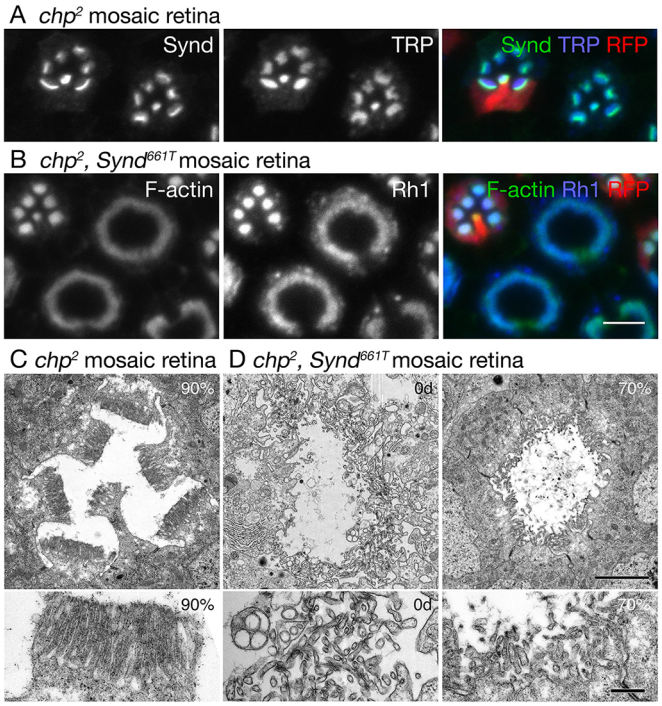

Fig. 8. Loss of Chp strongly enhances the disruption of stalk-rhabdomere segregation caused by Synd deficiency. (A) Immunostaining of late pupal *chp*^{2} mosaic retinas using anti-Synd (green) and anti-TRP (blue) antibodies. RFP marks the wild-type photoreceptor. (B) Immunostaining of late pupal *chp*^{2} and *Synd*^{661T} double-mutant mosaic retinas using phalloidin (green) and anti-Rh1 antibody (blue). RFP marks the wild-type photoreceptor. (C,D) Cross-sections of an ommatidium (top) and microvilli (bottom) from the pupae at 90% pd *chp*^{2} homozygous ommatidium (C), and *chp*^{2} and *Synd*^{661T} double homozygous ommatidia (D) from 0 day adult flies or the pupae at 70% pd observed by electron microscopy. Two, three, two, three and four independent eyes were observed in A-D (0d) and D (70%), respectively. Scale bars: 5 µm in A,B; 2 µm in C,D (top); 200 nm in C,D (bottom).

chp^{2} and *Synd*^{661T} double-mutant ommatidia showed more severe disruption of stalk-rhabdomere separation than those in the *Synd*^{661T} or *chp*^{2} single-mutant ommatidia (Fig. S5E), resulting in smoother C-shaped figure of Rh1 staining (Fig. 8B). Electron microscopy showed that microvilli showed no co-adherence but were spread across the entire apical membrane (Fig. 8D, left; 36/36 *chp*^{2}/*chp*^{2} *Synd*^{661T}/*Synd*^{661T} double-mutant photoreceptors). Moreover, in contrast to that of the *Synd*^{661T} single-mutant ommatidia (Fig. 6G), stalk-rhabdomere segregation was prominently disrupted even during mid-pupal development stage in the *chp*^{2} and *Synd*^{661T} double-mutant ommatidia (Fig. 8D, right; 27/27 *chp*^{2}/*chp*^{2} *Synd*^{661T}/*Synd*^{661T} double-mutant photoreceptors). During development of *chp*^{2} and *Synd*^{661T} double-mutant ommatidia, Crb and TRP colocalized at the apical membrane (Fig. S5E). Thus, severe defects of stalk and rhabdomere segregation in the *chp*^{2} and *Synd*^{661T} double-mutant photoreceptors were initiated before catacomb-like membrane architecture formation. These results implied that Chp and Synd are involved in distinct processes of stalk-rhabdomere segregation.

Endocytosis is not essential for stalk-rhabdomere segregation

As Synd has been reported to regulate endocytosis (Kessels and Qualmann, 2004; Seemann et al., 2017; Senju et al., 2011), we investigated whether endocytosis is required for stalk-rhabdomere segregation. We previously showed that endocytosed Rh1 accumulates in RLVs (Rh1-containing large vesicles). RNAi-knockdown of Rab5 in photoreceptors caused lack of RLVs, indicating that Rh1 endocytosis was totally inhibited; however, in these photoreceptors, the rhabdomere and stalk segregated properly, and Crb was restricted to the stalk membrane (Fig. S6A). *Shi*^{ts1} mutant flies kept at 29°C for 40 h also showed normal segregation of rhabdomere and stalk, although the rhabdomeres were partially degenerated, as reported previously (Pinal and Pichaud, 2011) (Fig. S6B). We also investigated the impact of the loss of endocytosis using clathrin heavy chain (Chc) DN and ChcRNAi, because clathrin pits are often observed on stalk membranes and at the base of rhabdomeres. In both photoreceptors, we found that rhabdomeres were small, but that rhabdomere-stalk separation was perfect. No Crb staining was seen in the rhabdomeres of dominant-negative protein of Chc (ChcDN)- or ChcRNAi-expressing photoreceptors (Fig. S6C,D). These results indicated that Synd is likely to contribute to the rhabdomere morphogenesis through its membrane curvature properties, rather than through endocytosis.

DISCUSSION

The present study shows that Synd loss leads to the failure of the microvilli to form a united bundle of rhabdomeres, resulting in small clusters of microvilli intermixed with stalk membrane. Super-resolution microscopy and electron micrograph indicated that Synd binds to the microvillar neck inner surface, presumably in a collar-like configuration. This forms and/or stabilizes the membrane curvature of the microvillar neck, which well fits the radius predicted from the *Drosophila* Synd dimer crystal structure (~21 nm) (Edeling et al., 2009). We also confirmed that p-Moe is required for proper segregation of the stalk and rhabdomere membrane (Karagiosis and Ready, 2004) through formation and/or stabilization of the rhabdomere base architecture. Synd and p-Moe appeared to colocalize at the rhabdomere base under conventional confocal microscopy. However, 2D-dSTORM super-resolution microscopy showed that the pattern of p-Moe localization is different from that of the regular array of Synd (Fig. 4I). Localization, function and membrane-binding nature of p-Moe imply the possibility of p-Moe localization on the base membrane around microvillar necks, where electron-dense spots were observed (Fig. 5B,E). Future research may provide more precise localization of p-Moe to connect these spots with p-Moe.

Here, we show one possible model of Synd and p-Moe localization and the organization of membrane architecture (Fig. 9). Synd localizes at the bottom of microvillus and p-Moe localizes between the microvilli, and both of them play crucial roles

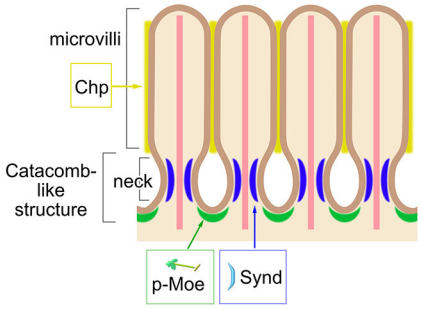

Fig. 9. Model of the rhabdomere base structure. Synd and p-Moe play crucial roles to support the structure of the rhabdomere base membrane, whereas Chp unites the microvilli to a rigid bundle: the rhabdomere. Synd (blue), p-Moe (green), Chp (yellow), plasma membrane (brown) and F-actin (pink). Schematics of the F-Bar-domain dimer of Synd and Moe are shown at a scale similar to that of the model.

Development (2019) 146, dev169292. doi:10.1242/dev.169292

to support the rhabdomere base structure and to exclude stalk membrane components, such as Crb.

We also found that Synd and p-Moe recruitment to the rhabdomere base were not co-dependent, and Moe^{PL54} and $Synd^{661T}$ double mutants did not exhibit a synergic or additive effect on stalk-rhabdomere segregation. These results indicate that Synd and Moe are independently required for the same process; namely, the catacomb-like architecture formation and/or stabilization at the rhabdomere base, which is required for stalk membrane elimination from the rhabdomere. Therefore, the lack of either of these proteins impairs stalk-rhabdomere segregation.

Pupal photoreceptors express another BAR protein, amphiphysin (Amph), which colocalizes with F-actin on the prospective rhabdomeres in young pupae (Zelhof et al., 2001). Amph-deficient adult photoreceptor rhabdomeres are tightly packed and occasionally fused, thus creating very little inter-rhabdomere space, indicating that Amph acts on rhabdomere morphogenesis. Together with the absence of Amph expression in adult photoreceptors, the phenotype difference between Amph and Synd indicated that Amph functions differently from Synd.

A well-known function of syndapin is the regulation of endocytosis. Thus, we investigated whether endocytosis is necessary for stalk-rhabdomere segregation; however, the stalk and rhabdomere separated perfectly in Rab5- and Chc-deficient photoreceptors. Thus, the function of Synd required in stalk-rhabdomere segregation is likely to be membrane curving, rather than endocytosis.

Polarized transport to the rhabdomeres is also unrelated to stalk-rhabdomere segregation. We have investigated many genes involved in vesicle transport in fly photoreceptors: Rab1 and Syx5 are involved in ER to Golgi transport; Rab6 is required for the transport between the TGN and RE; and Rab11/dRip11/MyoV are essential for the transport toward the rhabdomere. However, rhabdomere invasion by Crumbs was not observed in these mutants (Iwanami et al., 2016; Li et al., 2007; Satoh et al., 1997, 2005, 2016a,b). Nonetheless, Synd function in the transport to the stalk membrane cannot be excluded. Crumbs invasion of the rhabdomere might be explained if Synd blocks the access by Crumbs-bearing vesicles to the rhabdomere base membrane, by its concentrated localization at the base of the rhabdomere.

Chp is also required for the restricted localization of Crb on the stalk membrane, as Crb mislocalized to the rhabdomeres in the chp^2 mutant (Gurudev et al., 2014). We further found that additional loss of Chp significantly enhances the stalk-rhabdomere segregation defect of $Synd^{661T}$ deficiency. In chp^2 and $Synd^{661T}$ double-mutant ommatidia, individual microvilli were completely separated and spread across the apical membrane, indicating that Chp and Synd are required in distinct processes of stalk-rhabdomere segregation. As Chp is an adhesion molecule on the microvilli, this result suggests that microvilli bundling is one of the mechanisms for stalk and rhabdomere segregation. Our results indicate that this is powered by two independent microvilli bundling activities: (1) Chp-mediated adhesion over the entire microvillus length; and (2) scaffolding by Synd and p-Moe at the rhabdomere base membrane. These activities unify the microvilli into a single rhabdomere at the center of the apical membrane, concomitant with stalk membrane exclusion. As the stalk membrane is fragmented into the space between the clustered rhabdomere microvilli upon Synd or p-Moe loss, the stalk appeared not to have a mechanism to exclude microvilli or rhabdomere base membrane, despite the F-actin and β-spectrin network supporting the stalk membrane.

A stereocilium of the hair cell of the mammalian cochlea is a structure equivalent to the fly photoreceptor microvillus. The base of the stereocilium is also constricted and forms a neck. Protocadherin 15 (PCDH15) forms links that connect neighboring stereocilia, and the bundle of stereocilia forms a single domain within the apical surface. In the zebrafish, syndapin 1 and cordon bleu (Cobl) are required for both microtubule-dependent kinocilia and F-actin-rich stereocilia formation, and both proteins localize to the base of developing cilia in ZF4 cells (Schüler et al., 2013). Syndapin and another Bar protein, ASAP1, are recruited to the microvillus base by Cobl overexpression in Jeg3 cells (Grega-Larson et al., 2015). Thus, syndapin localization on the microvillus or stereocilia neck appears to be a general feature. Mutations in *FAM65B* (*RIPOR2*) cause hearing loss in humans (Diaz-Horta et al., 2014). Fam65b forms ring-like structures at the stereocilia base (Zhao et al., 2016); this configuration resembles the distribution of electron-dense spots in our electron microscopic analysis (Fig. 5E). Without Fam65b, the stereocilia are not tightly bundled and each stereocilium points in a different direction. This phenotype is similar to that of $Synd^{661T}$ homozygous mutant fly photoreceptors (Zhao et al., 2016). Notably, a DNA sequence comparison suggested Fam65b might have a PX-Bar domain (Diaz-Horta et al., 2014); however, this conclusion has been contested (Teasdale and Collins, 2014). Neck formation to constrict the plasma membrane by BAR proteins might be a general mechanism for microvilli-mediated formation of the domain.

MATERIALS AND METHODS

Drosophila stocks and genetic backgrounds

The flies were grown at 18-25°C on standard cornmeal-glucose-agar-yeast food. The EMS mutagenesis and F_2 live-imaging screening were performed as described previously (Iwanami et al., 2016). The starter strain with the second chromosome carrying proximal neoFRT at 82B was isogenized from the Bloomington Stock #5619, which was used in single nucleotide polymorphism (SNP) mapping (Berger et al., 2001). The tester line *w; Rh1Arr2GFP ey-FLP/SM1; FRT82B P3RFP/TM6B* was used for live imaging of mutant lines. *y w ey-FLP::FRT82B P3RFP* was used for immunostaining. $Synd^{mut1}$, *BSC43* (deficiency for Synd region) was provided by Dr Takeda (Okayama University, Japan). moe^{PL54}, *FRT19A* and *UAS-moe::GFP* were provided by Dr Payre (Centre de Biologie du Développement, Université Paul Sabatier, Toulouse, France). $slik^1$ was provided by Dr Hipfner [Institut de Recherches Cliniques de Montréal (IRCM), Canada]. chp^2 (BL42251), $w\ shi^{ts1}$ (BL7068), *UAS-ChcDN* (BL26847) and *w;; UAS-ChcRNAi* (BL27530) were obtained from the Bloomington *Drosophila* Stock Center. $Rab5RNAi^{GD10492}$ (*v34096*) was obtained from the Vienna *Drosophila* Resource Center. The following Gal4 lines were used: Rh1-Gal4 (a gift from Dr Hama, Kyoto Sangyo University, Kyoto, Japan), and heat shock-Gal4 and GMR-Gal4 (obtained from the Bloomington Stock Center).

Live imaging of fluorescent proteins expressed in photoreceptors

The fluorescent proteins expressed in the photoreceptors were imaged by the water-immersion technique as described previously (Satoh et al., 2013).

Immunohistochemistry

The fixation and staining methods were performed as described previously (Satoh and Ready, 2005). Primary antisera used were as follows: rabbit anti-Rh1 (1:1000) (Satoh et al., 2005), chicken anti-Rh1 (1:1000) (Satoh et al., 2013), mouse monoclonal anti-Na^+K^+ATPase alpha subunit (1:500 ascites) (Developmental Study Hybridoma Bank), rat monoclonal anti-DE-Cad (1:15 supernatant) (DSHB), rat anti-Crb (1:300) (a gift from Dr Tepass, University of Toronto, Canada), rabbit anti-TRP (1/1000) (a gift from Dr Montell, Johns Hopkins University, Baltimore, MD, USA), mouse monoclonal anti-Arm (1:15 supernatant) (DSHB), anti-phosphorylated ERM (p-Moe) (1/300, high conc: 1/12) (Cell Signaling Technology Japan, Tokyo, Japan; #3141S), guinea pig anti-Slik (1/300) (a gift from

Development (2019) 146, dev169292. doi:10.1242/dev.169292

Dr Hipfner), rabbit anti-Synd (1/100) (prepared for this study) and mouse anti-Synd (1/100, high conc: 1/40) (prepared for this study). The secondary antibodies included anti-mouse, anti-rabbit, anti-rat and/or anti-chicken antibodies labeled with Alexa Fluor 488, 568 or 647 (1:300, high conc: 1/100) [Life Technologies, A-21202 (mouse 488), A-11008 (rabbit 488), A-11006 (rat 488), A-11039 (chicken 488), A10037 (mouse 568), A-11036 (rabbit 568), A-11077 (rat 568), A-11041 (chicken 568), A31571 (mouse 647), A-21245 (rabbit 647), A-21247 (rat 647), A-21449 (chicken 647)]. The images of samples were recorded using an FV1000 confocal microscope (60×1.42 NA objective lens; Olympus). To minimize bleed-through, each signal in double- or triple-stained sample was imaged sequentially. The images were processed in accordance with the Guidelines for Proper Digital Image Handling using ImageJ and/or Adobe Photoshop CS3.

Electron microscopy

Electron microscopy was performed as described previously (Satoh et al., 1997). The samples were observed using a JEM1400 electron microscope (JEOL) and montage images were taken using a CCD camera system (JEOL). Intensities along the concentric circles for various radiuses were plotted using ImageJ.

Mapping and determination of mutations

Meiotic recombination mapping between proximal FRT at 82B, 661T-responsible mutation and distal miniature w^+ marker *P{EP318}* at 100D2 (Berger et al., 2001) was carried out. The isogenized *y w ey-FLP;; FRT82B 661T/TM6B* flies were crossed with *y w ey-FLP;; P{EP0511}* flies isogenized from the Bloomington stock #6414. The female offspring carrying the mutated chromosome and miniature w^+-marked chromosome was crossed with *y w ey-FLP; Rh1Arr2GFP; FRT82B P3RFP* males with an isogenized third chromosome. The offspring with w^+ mosaic eyes were considered as *FRT82B-EP318* recombinants. Using the confocal live imaging of Arr2::GFP, the inheritance of C-shaped rhabdomeres of each recombinant was determined. The recovered recombinant flies were individually placed in 50 µl of 200 ng/µl proteinase K in 10 mM Tris-chloride (Tris-Cl) (pH 8.2), 1 mM EDTA and 25 mM sodium chloride (NaCl), and then digested at 55°C for 1 h. The digestion was stopped by heat inactivation at 85°C for 30 min and 95°C for 5 min. Subsequently, a 0.5 µl aliquot of the digested solution was used as the template for PCR amplification for RFLP analysis as described in the FlySNP database (Chen et al., 2008).

Whole-genome resequencing of EMS-generated mutants

For whole-genome resequencing of the 661T mutant, the genomic DNA was extracted from homozygotes of isogenized starter third chromosome FRT82B, and heterozygous males of 661T and FRT82B. The DNA libraries were prepared using the NEB Next DNA Library Prep Set for SOLiD (New England Biolabs). The paired-end 75+35 bp reads were obtained using the SOLiD 5500xl (Applied Biosystems), converted to fastq format, and mapped to the release 5 genome of the *D. melanogaster* genome using BWA 0.5.9 (Li and Durbin, 2009). The single nucleotide variants (SNVs) and indels were called using the Genome Analysis Tool Kit 2.1 (GATK, Broad Institute, Cambridge, MA, USA), and annotated using SnpSift (Cingolani et al., 2012). The RFLP-mapped region of the 661T mutant was covered by reads with an average depth of ×38. Molecularly defined chromosomal deletions (i.e. *ED5942*, *BSC475*, *BSC809*, *BSC818*, *Exel6184*, *BSC808*, *ED6025*, *ED6027*, *BSC517*, *BSC516*, *Exel6185*, *BSC518*, *BSC488*, *BSC141*, *BSC124*, *BSC819*, *BSC680*, *ED10811*, *ED10820* and *Exel6272*) were used for complementation tests with the 661 T mutant. NGS data of Starter *FRT82B* and *661T* mutant are available at Figshare (doi.org/10.6084/m9.figshare.7421636).

Generation of anti-Synd antibodies

One rabbit and five mice anti-Synd polyclonal antisera were generated against a unique Synd region near the N-terminal peptide (amino acids 15-32: DSF) (Sigma Aldrich).

Immunoblotting

Immunoblotting was performed as described previously (Satoh et al., 1997). The following antibodies were used: rabbit anti-Synd (1:1000) (prepared for this study), mouse anti-Synd (1:1000) (prepared for this study) and chicken anti-Arr2 (1:40,000) (Satoh et al., 2010). Horseradish peroxidase-conjugated anti-rabbit and anti-mouse IgG antibodies (1:20,000, Life Technologies, 115-035-003, 111-035-003) were used as secondary antibodies. The signals were visualized by enhanced chemiluminescence (Clarity Western ECL Substrate; Bio-Rad) and imaged using ChemiDoc XRS+ (Bio-Rad).

Super-resolution imaging

To suppress autofluorescence, the flies were raised in vitamin A-deficient media. The mosaic retinas from late pupae of *y w ey-FLP;;FRT82B/FRT82B* $Synd^{661T}$ were dissected, rubbed on 35 mm microdishes with ibiTreat (ibidi) and the separated ommatidia were fixed in 4% paraformaldehyde in periodate-lysine-paraformaldehyde buffer for 3 min, washed in phosphate-buffered saline (PBS) and permeabilized in PBS with 0.1% Triton X-1000 for 5 min. Immunostaining was performed as described above using mouse anti-Synd antibody (1/40) and goat anti-mouse IgG labeled with Alexa Fluor 647 (1/100). 2D-dSTORM was performed using Delta Vision OMX V3 microscope (GE Healthcare) with a silicone immersion objective lens (UPLSAPO 100XS NA 1.35; Olympus). For 2D-dSTORM, the conventional light path without TIRF was used as the rhabdomeres were not directly on the coverslip surface. About 20-30 min before imaging, the sample solution was replaced with the imaging buffer containing 60 mM HEPES (pH 7.6), 0.6× PBS, 0.5 mg/ml glucose oxidase, 40 µg/ml catalase, 5% glucose and 143 mM 2-mercaptoethanol. For two-color 2D-dSTORM, mouse anti-Synd (1/40) and rabbit anti-phosphorylated ERM (p-Moe) (1/12) (Cell Signaling Technology) were used as primary antibodies, and Alexa Fluor 568-labeled anti-mouse IgG (1/100) and Alexa Fluor 647-labeled anti-rabbit IgG (1/100) were used as secondary antibodies. For Synd and Synd-GFP double labeling, mosaic retina from pupae of *w; UAS-Synd::GFP/hs-Gal4 ey-FLP ; FRT82B/FRT82B* $Synd^{661T}$ were immunostained using mouse anti-Synd (1/40) and chicken anti-GFP (1/100) antibodies followed by goat Alexa Fluor 568 anti-mouse IgG (1/100) and Alexa Fluor 647 anti-chicken antibody (1/100). Two channels were simultaneously obtained using two EM-CCDs as in single-color d2D-STORM and individually reconstructed. Image frames of 30,000-53,000 were denoised and deconvolved to increase resolution in noisy images (Matsuda et al., 2010), and reconstructed using DAOSTORM (Holden et al., 2011). Sample drift was corrected by iterative cross-correlation of time projection of 1000 frames of the original STORM images. To superimpose the two-color images, a reference image using bleed-through of shorter wavelength was obtained before 2D-dSTORM imaging and used to calculate the registration parameters using Chromagnon v0.64 software (Matsuda et al., 2018). To find the peak coordinates, Priism suite (https://biii.eu/priismive) was used with a threshold at 150 times of the standard deviation of the overall signal, and minimum point separation at 1 pixel (10 nm). Multicolor 2D-dSTORM images were shown with a gamma value of 0.6 for Synd and 0.9 for Moe or Synd-GFP.

Acknowledgements

We thank Dr U. Tepass, Dr C. Montell, and Dr D. Hipfner for kindly providing the fly stocks and reagents. We also thank the Bloomington Stock Center and the Drosophila Genetic Resource Center (Kyoto Institute of Technology) for the fly stocks. The whole-genome and targeted gene resequencing was carried out at the Center for Gene Research, Nagoya University. We also thank Editage (www.editage.jp) for English language editing.

Competing interests

The authors declare no competing or financial interests.

Author contributions

Conceptualization: A.K.S., T.S.; Methodology: A.M.; Validation: A.K.S., T.S.; Investigation: A.K.S., S.O., Y.O., Z.L., T.S.; Data curation: S.O., A.M., T.S.; Writing - original draft: A.K.S., T.S.; Supervision: A.K.S., T.S.; Project administration: A.K.S., T.S.; Funding acquisition: A.K.S.

Funding

This work was supported by Precursory Research for Embryonic Science and Technology (grant number 25-J-J4215), by the Japan Society for the Promotion of

Science, KAKENHI (grant number 15K07050) and by the Yamada Science Foundation, Daiichi Sankyo Foundation of Life Science (to A.K.S.).

Data availability

dSTORM images of rhabdomeres are available in Figshare (doi.org/10.6084/m9.figshare.7427966).

Supplementary information

Supplementary information available online at
http://dev.biologists.org/lookup/doi/10.1242/dev.169292.supplemental

References

Berger, J., Suzuki, T., Senti, K.-A., Stubbs, J., Schaffner, G. and Dickson, B. J. (2001). Genetic mapping with SNP markers in Drosophila. *Nat. Genet.* **29**, 475-481. doi:10.1038/ng773

Bulgakova, N. A., Kempkens, O. and Knust, E. (2008). Multiple domains of Stardust differentially mediate localisation of the Crumbs-Stardust complex during photoreceptor development in Drosophila. *J. Cell Sci.* **121**, 2018-2026. doi:10.1242/jcs.031088

Bulgakova, N. A., Rentsch, M. and Knust, E. (2010). Antagonistic functions of two stardust isoforms in Drosophila photoreceptor cells. *Mol. Biol. Cell* **21**, 3915-3925. doi:10.1091/mbc.e09-10-0917

Chen, D., Ahlford, A., Schnorrer, F., Kalchhauser, I., Fellner, M., Viràgh, E., Kiss, I., Syvänen, A.-C. and Dickson, B. J. (2008). High-resolution, high-throughput SNP mapping in Drosophila melanogaster. *Nat. Methods* **5**, 323-329. doi:10.1038/nmeth.1191

Cingolani, P., Patel, V. M., Coon, M., Nguyen, T., Land, S. J., Ruden, D. M. and Lu, X. (2012). Using Drosophila melanogaster as a model for genotoxic chemical mutational studies with a new program, SnpSift. *Front. Genet.* **3**, 35. doi:10.3389/fgene.2012.00035

Diaz-Horta, O., Subasioglu-Uzak, A., Grati, M., DeSmidt, A., Foster, J., Cao, L., Bademci, G., Tokgoz-Yilmaz, S., Duman, D., Cengiz, F. B. et al. (2014). FAM65B is a membrane-associated protein of hair cell stereocilia required for hearing. *Proc. Natl. Acad. Sci. USA* **111**, 9864-9868. doi:10.1073/pnas.1401950111

Dorland, Y. L., Malinova, T. S., van Stalborch, A.-M. D., Grieve, A. G., van Geemen, D., Jansen, N. S., de Kreuk, B.-J., Nawaz, K., Kole, J., Geerts, D. et al. (2016). The F-BAR protein pacsin2 inhibits asymmetric VE-cadherin internalization from tensile adherens junctions. *Nat. Commun.* **7**, 12210. doi:10.1038/ncomms12210

Edeling, M. A., Sanker, S., Shima, T., Umasankar, P. K., Höning, S., Kim, H. Y., Davidson, L. A., Watkins, S. C., Tsang, M., Owen, D. J. et al. (2009). Structural requirements for PACSIN/Syndapin operation during zebrafish embryonic notochord development. *PLoS ONE* **4**, e8150. doi:10.1371/journal.pone.0008150

Fehon, R. G., McClatchey, A. I. and Bretscher, A. (2010). Organizing the cell cortex: the role of ERM proteins. *Nat. Rev. Mol. Cell Biol.* **11**, 276-287. doi:10.1038/nrm2866

Flores-Benitez, D. and Knust, E. (2016). Dynamics of epithelial cell polarity in Drosophila: how to regulate the regulators? *Curr. Opin. Cell Biol.* **42**, 13-21. doi:10.1016/j.ceb.2016.03.018

Gleason, A. M., Nguyen, K. C. Q., Hall, D. H. and Grant, B. D. (2016). Syndapin/SDPN-1 is required for endocytic recycling and endosomal actin association in the C. elegans intestine. *Mol. Biol. Cell* **27**, 3687-3790. doi:10.1091/mbc.e16-02-0116

Grega-Larson, N. E., Crawley, S. W., Erwin, A. L. and Tyska, M. J. (2015). Cordon bleu promotes the assembly of brush border microvilli. *Mol. Biol. Cell* **26**, 3803-3815. doi:10.1091/mbc.E15-06-0443

Gurudev, N., Yuan, M. and Knust, E. (2014). chaoptin, prominin, eyes shut and crumbs form a genetic network controlling the apical compartment of Drosophila photoreceptor cells. *Biol. Open* **3**, 332-341. doi:10.1242/bio.20147310

Heilemann, M., van de Linde, S., Schüttpelz, M., Kasper, R., Seefeldt, B., Mukherjee, A., Tinnefeld, P. and Sauer, M. (2008). Subdiffraction-resolution fluorescence imaging with conventional fluorescent probes. *Angew. Chem. Int. Ed. Engl.* **47**, 6172-6176. doi:10.1002/anie.200802376

Hipfner, D. R., Keller, N. and Cohen, S. M. (2004). Slik Sterile-20 kinase regulates Moesin activity to promote epithelial integrity during tissue growth. *Genes Dev.* **18**, 2243-2248. doi:10.1101/gad.303304

Holden, S. J., Uphoff, S. and Kapanidis, A. N. (2011). DAOSTORM: an algorithm for high- density super-resolution microscopy. *Nat. Methods* **8**, 279-280. doi:10.1038/nmeth0411-279

Hong, Y., Ackerman, L., Jan, L. Y. and Jan, Y.-N. (2003). Distinct roles of Bazooka and Stardust in the specification of Drosophila photoreceptor membrane architecture. *Proc. Natl. Acad. Sci. USA* **100**, 12712-12717. doi:10.1073/pnas.2135347100

Hughes, S. C. and Fehon, R. G. (2006). Phosphorylation and activity of the tumor suppressor Merlin and the ERM protein Moesin are coordinately regulated by the Slik kinase. *J. Cell Biol.* **175**, 305-313. doi:10.1083/jcb.200608009

Hughes, S. C., Formstecher, E. and Fehon, R. G. (2010). Sip1, the Drosophila orthologue of EBP50/NHERF1, functions with the sterile 20 family kinase Slik to regulate Moesin activity. *J. Cell Sci.* **123**, 1099-1107. doi:10.1242/jcs.059469

Iwanami, N., Nakamura, Y., Satoh, T., Liu, Z. and Satoh, A. K. (2016). Rab6 is required for multiple apical transport pathways but not the basolateral transport pathway in Drosophila photoreceptors. *PLoS Genet.* **12**, e1005828. doi:10.1371/journal.pgen.1005828

Izaddoost, S., Nam, S.-C., Bhat, M. A., Bellen, H. J. and Choi, K.-W. (2002). Drosophila Crumbs is a positional cue in photoreceptor adherens junctions and rhabdomeres. *Nature* **416**, 178-183. doi:10.1038/nature720

Karagiosis, S. A. and Ready, D. F. (2004). Moesin contributes an essential structural role in Drosophila photoreceptor morphogenesis. *Development* **131**, 725-732. doi:10.1242/dev.00976

Kessels, M. M. and Qualmann, B. (2004). The syndapin protein family: linking membrane trafficking with the cytoskeleton. *J. Cell Sci.* **117**, 3077-3086. doi:10.1242/jcs.01290

Kumar, J. P. and Ready, D. F. (1995). Rhodopsin plays an essential structural role in Drosophila photoreceptor development. *Development* **121**, 4359-4370.

Kumar, V., Alla, S. R., Krishnan, K. S. and Ramaswami, M. (2009a). Syndapin is dispensable for synaptic vesicle endocytosis at the Drosophila larval neuromuscular junction. *Mol. Cell. Neurosci.* **40**, 234-241. doi:10.1016/j.mcn.2008.10.011

Kumar, V., Fricke, R., Bhar, D., Reddy-Alla, S., Krishnan, K. S., Bogdan, S. and Ramaswami, M. (2009b). Syndapin promotes formation of a postsynaptic membrane system in Drosophila. *Mol. Biol. Cell* **20**, 2254-2264. doi:10.1091/mbc.e08-10-1072

Laprise, P. and Tepass, U. (2011). Novel insights into epithelial polarity proteins in Drosophila. *Trends Cell Biol.* **21**, 401-408. doi:10.1016/j.tcb.2011.03.005

Li, H. and Durbin, R. (2009). Fast and accurate short read alignment with Burrows-Wheeler transform. *Bioinformatics* **25**, 1754-1760. doi:10.1093/bioinformatics/btp324

Li, B. X., Satoh, A. K. and Ready, D. F. (2007). Myosin V, Rab11, and dRip11 direct apical secretion and cellular morphogenesis in developing Drosophila photoreceptors. *J. Cell Biol.* **177**, 659-669. doi:10.1083/jcb.200610157

Liu, L.-Y., Lin, C.-H. and Fan, S.-S. (2009). Function of Drosophila mob2 in photoreceptor morphogenesis. *Cell Tissue Res.* **338**, 377-389. doi:10.1007/s00441-009-0878-7

Longley, R. L. and Ready, D. F. (1995). Integrins and the development of three-dimensional structure in the Drosophila compound eye. *Dev. Biol.* **171**, 415-433. doi:10.1006/dbio.1995.1292

Matsuda, A., Shao, L., Boulanger, J., Kervrann, C., Carlton, P. M., Kner, P., Agard, D. and Sedat, J. W. (2010). Condensed mitotic chromosome structure at nanometer resolution using PALM and EGFP- histones. *PLoS ONE* **5**, e12768. doi:10.1371/journal.pone.0012768

Matsuda, A., Schermelleh, L., Hirano, Y., Haraguchi, T. and Hiraoka, Y. (2018). Accurate and fiducial-marker-free correction for three-dimensional chromatic shift in biological fluorescence microscopy. *Sci. Rep.* **8**, 7583. doi:10.1038/s41598-018-25922-7

McClatchey, A. I. (2014). ERM proteins at a glance. *J. Cell Sci.* **127**, 3199-3204. doi:10.1242/jcs.098343

Nam, S.-C. and Choi, K. W. (2003). Interaction of Par-6 and Crumbs complexes is essential for photoreceptor morphogenesis in Drosophila. *Development* **130**, 4363-4372. doi:10.1242/dev.00648

Nam, S.-C. and Choi, K.-W. (2006). Domain-specific early and late function of Dpatj in Drosophila photoreceptor cells. *Dev. Dyn.* **235**, 1501-1507. doi:10.1002/dvdy.20726

Oh, E. and Robinson, I. (2012). Barfly: sculpting membranes at the Drosophila neuromuscular junction. *Dev. Neurobiol.* **72**, 33-56. doi:10.1002/dneu.20923

Pellikka, M., Tanentzapf, G., Pinto, M., Smith, C., McGlade, C. J., Ready, D. F. and Tepass, U. (2002). Crumbs, the Drosophila homologue of human CRB1/RP12, is essential for photoreceptor morphogenesis. *Nature* **416**, 143-149. doi:10.1038/nature721

Pérez-Otaño, I., Luján, R., Tavalin, S. J., Plomann, M., Modregger, J., Liu, X.-B., Jones, E. G., Heinemann, S. F., Lo, D. C. and Ehlers, M. D. (2006). Endocytosis and synaptic removal of NR3A-containing NMDA receptors by PACSIN1/syndapin1. *Nat. Neurosci.* **9**, 611-621. doi:10.1038/nn1680

Pichaud, F. (2018). PAR-complex and crumbs function during photoreceptor morphogenesis and retinal degeneration. *Front. Cell Neurosci.* **12**, 90. doi:10.3389/fncel.2018.00090

Pinal, N. and Pichaud, F. (2011). Dynamin- and Rab5-dependent endocytosis is required to prevent Drosophila photoreceptor degeneration. *J. Cell Sci.* **124**, 1564-1570. doi:10.1242/jcs.082115

Quan, A. and Robinson, P. J. (2013). Syndapin–a membrane remodelling and endocytic F-BAR protein. *FEBS J.* **280**, 5198-5212. doi:10.1111/febs.12343

Reinke, R., Krantz, D. E., Yen, D. and Zipursky, S. L. (1988). Chaoptin, a cell surface glycoprotein required for Drosophila photoreceptor cell morphogenesis, contains a repeat motif found in yeast and human. *Cell* **52**, 291-301. doi:10.1016/0092-8674(88)90518-1

Rodriguez-Boulan, E. and Macara, I. G. (2014). Organization and execution of the epithelial polarity programme. *Nat. Rev. Mol. Cell Biol.* **15**, 225-242. doi:10.1038/nrm3775

Satoh, A. K. and Ready, D. F. (2005). Arrestin1 mediates light-dependent rhodopsin endocytosis and cell survival. *Curr. Biol.* **15**, 1722-1733. doi:10.1016/j.cub.2005.08.064

Satoh, A., Tokunaga, F., Kawamura, S. and Ozaki, K. (1997). In situ inhibition of vesicle transport and protein processing in the dominant negative Rab1 mutant of Drosophila. *J. Cell Sci.* **110**, 2943-2953.

Satoh, A. K., O'Tousa, J. E., Ozaki, K. and Ready, D. F. (2005). Rab11 mediates post-Golgi trafficking of rhodopsin to the photosensitive apical membrane of Drosophila photoreceptors. *Development* **132**, 1487-1497. doi:10.1242/dev.01704

Satoh, A. K., Xia, H., Yan, L., Liu, C.-H., Hardie, R. C. and Ready, D. F. (2010). Arrestin translocation is stoichiometric to rhodopsin isomerization and accelerated by phototransduction in Drosophila photoreceptors. *Neuron* **67**, 997-1008. doi:10.1016/j.neuron.2010.08.024

Satoh, T., Inagaki, T., Liu, Z., Watanabe, R. and Satoh, A. K. (2013). GPI biosynthesis is essential for rhodopsin sorting at the trans-Golgi network in Drosophila photoreceptors. *Development* **140**, 385-394. doi:10.1242/dev.083683

Satoh, T., Nakamura, Y. and Satoh, A. K. (2016a). Rab6 functions in polarized transport in Drosophila photoreceptors. *Fly* **10**, 123-127. doi:10.1080/19336934.2016.1182273

Satoh, T., Nakamura, Y. and Satoh, A. K. (2016b). The roles of Syx5 in Golgi morphology and Rhodopsin transport in Drosophila photoreceptors. *Biol. Open* **5**, 1420-1430. doi:10.1242/bio.020958

Schneider, K., Seemann, E., Liebmann, L., Ahuja, R., Koch, D., Westermann, M., Hübner, C. A., Kessels, M. M. and Qualmann, B. (2014). ProSAP1 and membrane nanodomain-associated syndapin I promote postsynapse formation and function. *J. Cell Biol.* **205**, 197-215. doi:10.1083/jcb.201307088

Schüler, S., Hauptmann, J., Perner, B., Kessels, M. M., Englert, C. and Qualmann, B. (2013). Ciliated sensory hair cell formation and function require the F-BAR protein syndapin I and the WH2 domain-based actin nucleator Cobl. *J. Cell Sci.* **126**, 196-208. doi:10.1242/jcs.111674

Seemann, E., Sun, M., Krueger, S., Tröger, J., Hou, W., Haag, N., Schüler, S., Westermann, M., Huebner, C. A., Romeike, B. et al. (2017). Deciphering caveolar functions by *syndapin III* KO-mediated impairment of caveolar invagination. *eLife* **6**, e29854. doi:10.7554/eLife.29854

Senju, Y., Itoh, Y., Takano, K., Hamada, S. and Suetsugu, S. (2011). Essential role of PACSIN2/syndapin-II in caveolae membrane sculpting. *J. Cell Sci.* **124**, 2032-2040. doi:10.1242/jcs.086264

Sherlekar, A. and Rikhy, R. (2016). Syndapin promotes pseudocleavage furrow formation by actin organization in the syncytial Drosophila embryo. *Mol. Biol. Cell* **27**, 2064-2079. doi:10.1091/mbc.E15-09-0656

Shimada, A., Niwa, H., Tsujita, K., Suetsugu, S., Nitta, K., Hanawa-Suetsugu, K., Akasaka, R., Nishino, Y., Toyama, M., Chen, L. et al. (2007). Curved EFC/F-BAR-domain dimers are joined end to end into a filament for membrane invagination in endocytosis. *Cell* **129**, 761-772. doi:10.1016/j.cell.2007.03.040

Shimada, A., Takano, K., Shirouzu, M., Hanawa-Suetsugu, K., Terada, T., Toyooka, K., Umehara, T., Yamamoto, M., Yokoyama, S. and Suetsugu, S. (2010). Mapping of the basic amino-acid residues responsible for tubulation and cellular protrusion by the EFC/F-BAR domain of pacsin2/Syndapin II. *FEBS Lett.* **584**, 1111-1118. doi:10.1016/j.febslet.2010.02.058

Suetsugu, S. and Itoh, Y. (2012). BAR domain superfamily proteins bind to the cellular membrane of various curvatures. *Seikagaku* **84**, 30-35.

Takeda, T., Robinson, I. M., Savoian, M. M., Griffiths, J. R., Whetton, A. D., McMahon, H. T. and Glover, D. M. (2013). Drosophila F-BAR protein Syndapin contributes to coupling the plasma membrane and contractile ring in cytokinesis. *Open Biol.* **3**, 130081. doi:10.1098/rsob.130081

Teasdale, R. D. and Collins, B. M. (2014). Little evidence that FAM65B belongs to the family of phox homology (PX) and bin/amphiphysin/rvs (BAR) domain-containing proteins. *Proc. Natl. Acad. Sci. USA* **111**, E4064. doi:10.1073/pnas.1412755111

Tepass, U. (2009). FERM proteins in animal morphogenesis. *Curr. Opin. Genet. Dev.* **19**, 357-367. doi:10.1016/j.gde.2009.05.006

Tepass, U. (2012). The apical polarity protein network in Drosophila epithelial cells: regulation of polarity, junctions, morphogenesis, cell growth, and survival. *Annu. Rev. Cell Dev. Biol.* **28**, 655-685. doi:10.1146/annurev-cellbio-092910-154033

Tepass, U. and Harris, K. P. (2007). Adherens junctions in Drosophila retinal morphogenesis. *Trends Cell Biol.* **17**, 26-35. doi:10.1016/j.tcb.2006.11.006

Thompson, R. E., Larson, D. R. and Webb, W. W. (2002). Precise nanometer localization analysis for individual fluorescent probes. *Biophys. J.* **82**, 2775-2783. doi:10.1016/S0006-3495(02)75618-X

Wang, Q., Navarro, M. V. A. S., Peng, G., Molinelli, E., Goh, S. L., Judson, B. L., Rajashankar, K. R. and Sondermann, H. (2009). Molecular mechanism of membrane constriction and tubulation mediated by the F-BAR protein Pacsin/Syndapin. *Proc. Natl. Acad. Sci. USA* **106**, 12700-12705. doi:10.1073/pnas.0902974106

Widagdo, J., Fang, H., Jang, S. E. and Anggono, V. (2016). PACSIN1 regulates the dynamics of AMPA receptor trafficking. *Sci. Rep.* **6**, 31070. doi:10.1038/srep31070

Yasuhara, J. C., Baumann, O. and Takeyasu, K. (2000). Localization of Na/K-ATPase in developing and adult Drosophila melanogaster photoreceptors. *Cell Tissue Res.* **300**, 239-249. doi:10.1007/s004410000195

Zelhof, A. C., Bao, H., Hardy, R. W., Razzaq, A., Zhang, B. and Doe, C. Q. (2001). Drosophila Amphiphysin is implicated in protein localization and membrane morphogenesis but not in synaptic vesicle endocytosis. *Development* **128**, 5005-5015.

Zhao, B., Wu, Z. and Müller, U. (2016). Murine Fam65b forms ring-like structures at the base of stereocilia critical for mechanosensory hair cell function. *eLife* **5**, e14222. doi:10.7554/eLife.14222

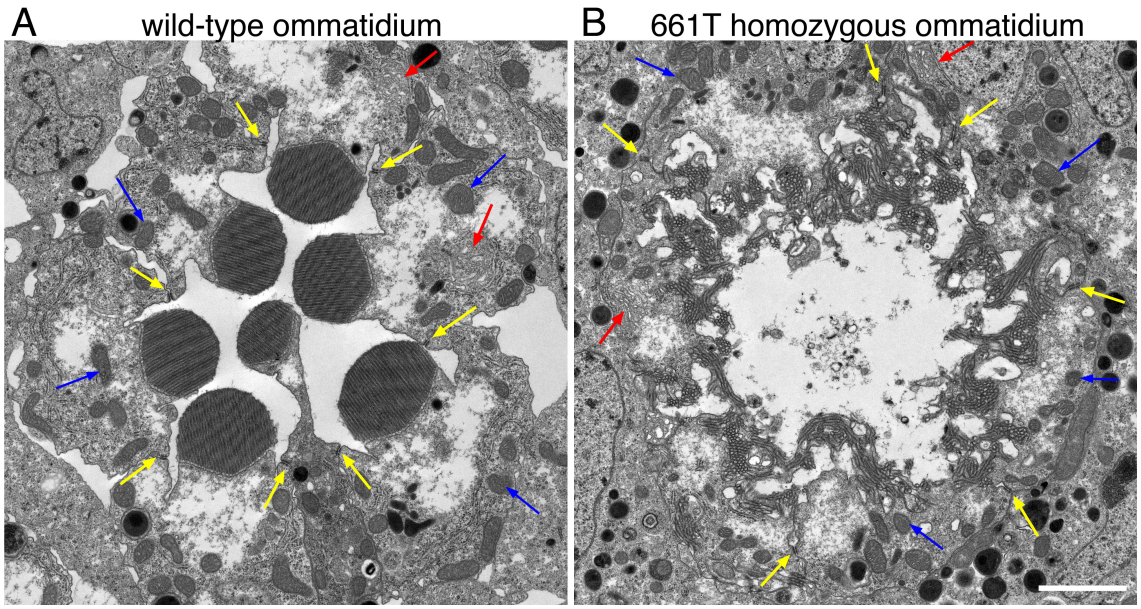

Fig. S1 Wild-type and 661T homozygous ommatidia at high resolution. Higher resolution of electron micrographs of the wild-type (A) and 661T homozygous ommatidia (B), shown in Fig. 1C and H. Yellow, red, and blue arrows indicate the adherens junctions, Golgi units, and mitochondria, respectively. Scale bar: 2 μm (A, B).

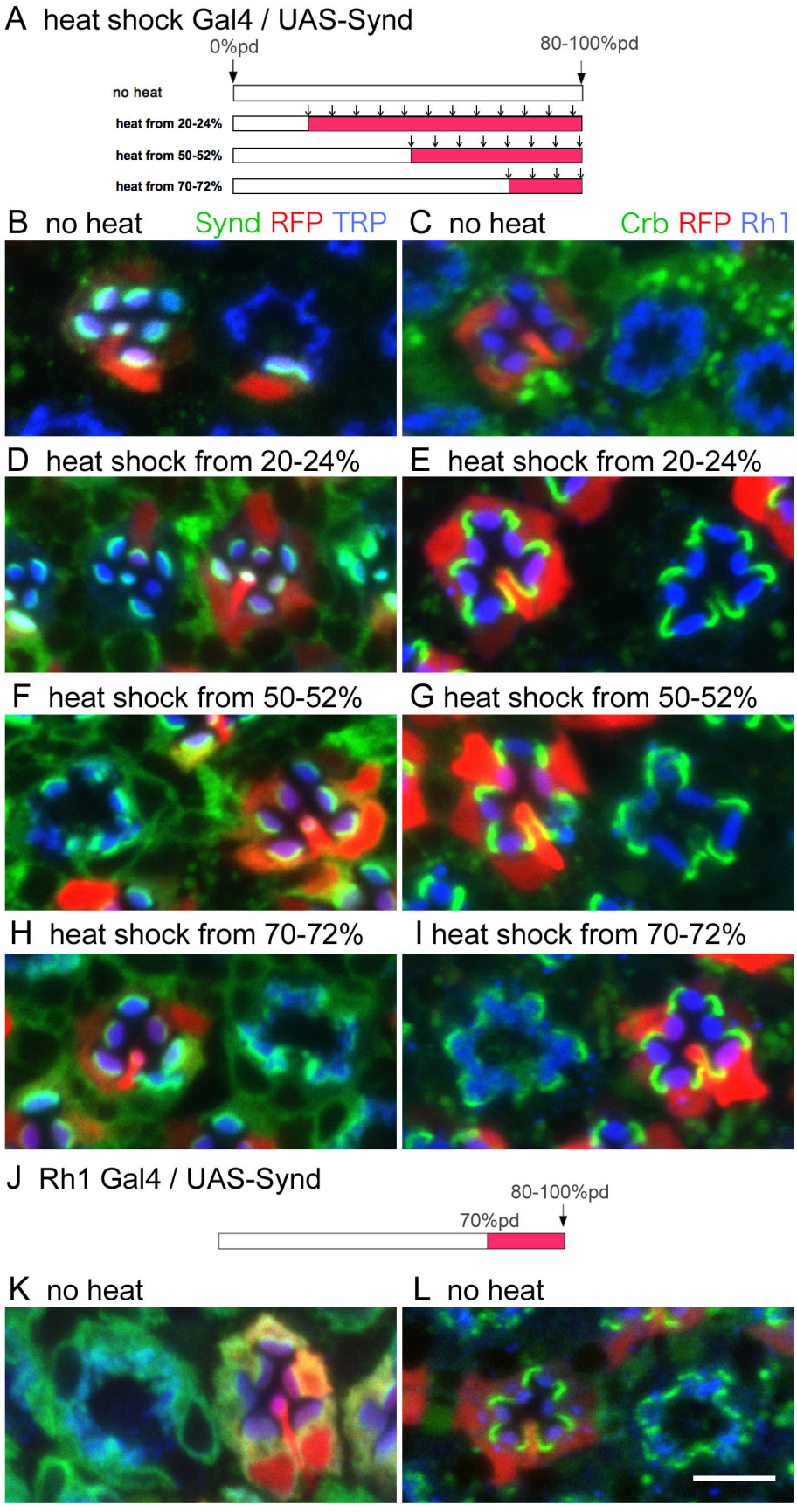

Fig. S2 Synd expression rescues the 661T mutant phenotype. Immunostaining of the late pupal 661T mutant mosaic eyes expressing Synd full length protein driven by a heat shock-Gal4 driver (B–I) or an Rh1-Gal4 driver (K, L). RFP (red) indicates wild-type cells. (A) Schematic representation of the heat shock procedure (arrow) and Synd expression (pink bar) driven by the heat shock-Gal4 driver. (J) Schematic representation of Synd expression (pink bar) driven by the Rh1-Gal4 driver. (B, D, F, H, K) Green represents Synd and blue represents TRP. (C, E, G, I, L) Green represents Crb and blue represents Rh1. 8, 6, 5, 5, 4, 4, 3, 4, 5 and 3 independent eyes were observed in B, C, D, E, F, G, H, I, K and L, respectively. Scale bar: 5 μm (B–I, K, L).

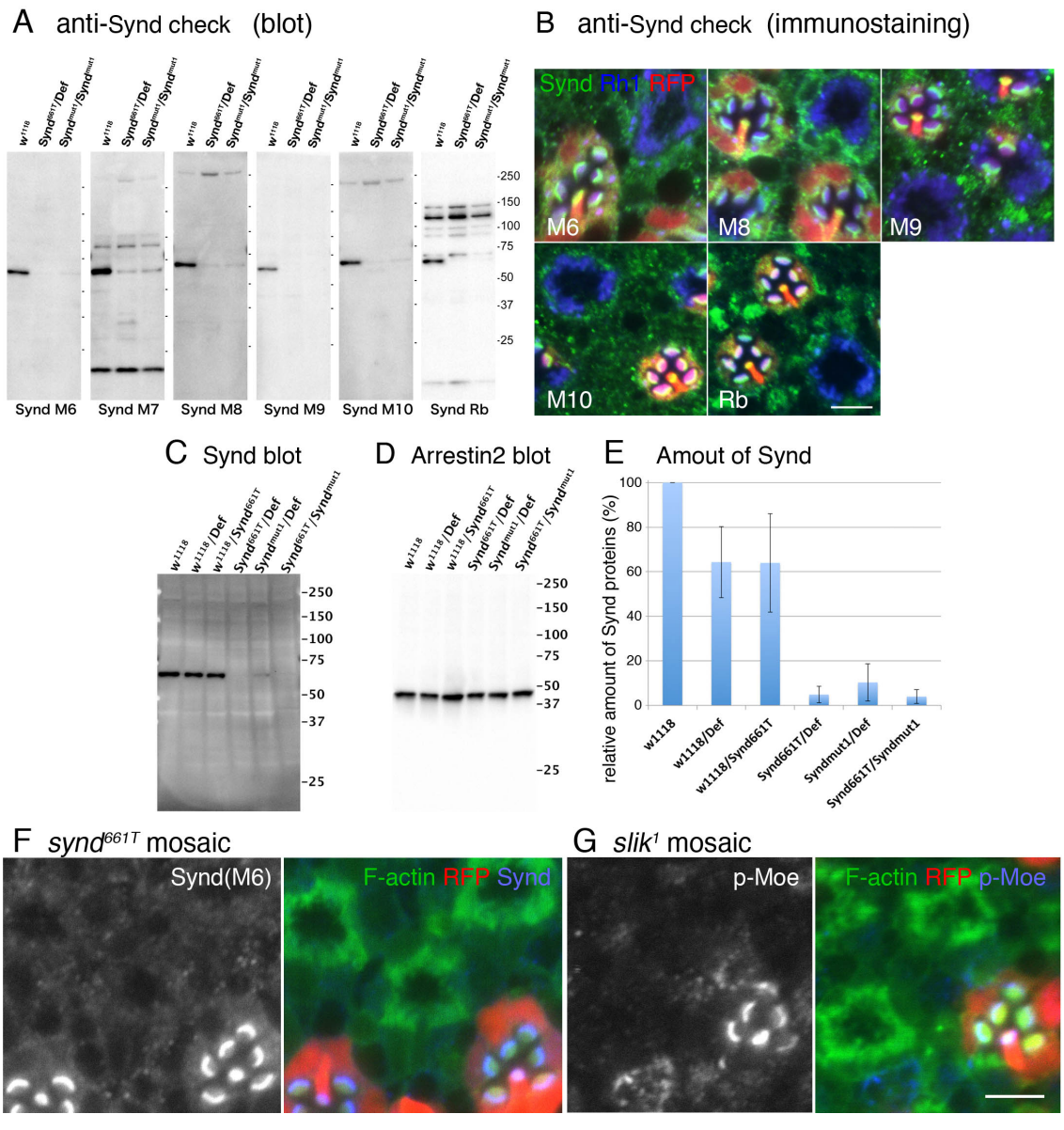

Fig. S3 Verification of anti-Synd and anti-Moe antisera, and characterization of the Synd^{661T} allele. (A) Immunoblotting of the fly head extracts of w^{1118} (wild-type), Synd^{661T}/Def, and Synd^{mut1} homozygous flies using mouse anti-Synd (M6-10) and rabbit anti-Synd (Rb) antibodies. (B) Immunostaining of the Synd^{661T} mutant mosaic eyes using mouse anti-Synd (M6, 8-10) and Rb anti-Synd antibodies (green). The mosaic eyes were also stained with Rh1 to visualize the rhabdomeres (blue). RFP (red) indicates wild-type cells. Scale bar: 5 μm. 1, 2, 2, 5 and 3 independent eyes were observed in M6, M8, M9, M10 and Rb, respectively. (C, D) Immunoblotting of the fly head extracts of w^{1118} (wild-type), w^{1118}/Def, w^{1118}/ Synd^{661T}, Synd^{661T}/Def, Synd^{mut1}/Def, and Synd^{661T}/Synd^{mut1} flies using mouse anti-Synd M6 (C) or anti-Arrestin2 antibodies (D). (E) Quantification of Synd normalized by Arrestin2 in the fly head extracts of w^{1118} (wild-type), w^{1118}/Def, w^{1118}/ Synd^{661T}, Synd^{661T}/Def, Synd^{mut1}/Def, and Synd^{661T}/Synd^{mut1} flies. Data are expressed as the means ± s.d. (n = 3). (F, G) Immunostaining of *Synd^{661T}* (F) and *Slik^{1}* (G) mutant mosaic eyes by high concentration of mouse anti-Synd (1/40) (F) or anti-pMoe antibodies (1/12) (blue) (G). Secondary antibodies are also used at high concentration (1/100). Phalloidin staining is shown in green. RFP (red) indicates wild-type cells. 9 and 7 independent eyes were observed in F and G, respectively. Scale bar: 5 μm.

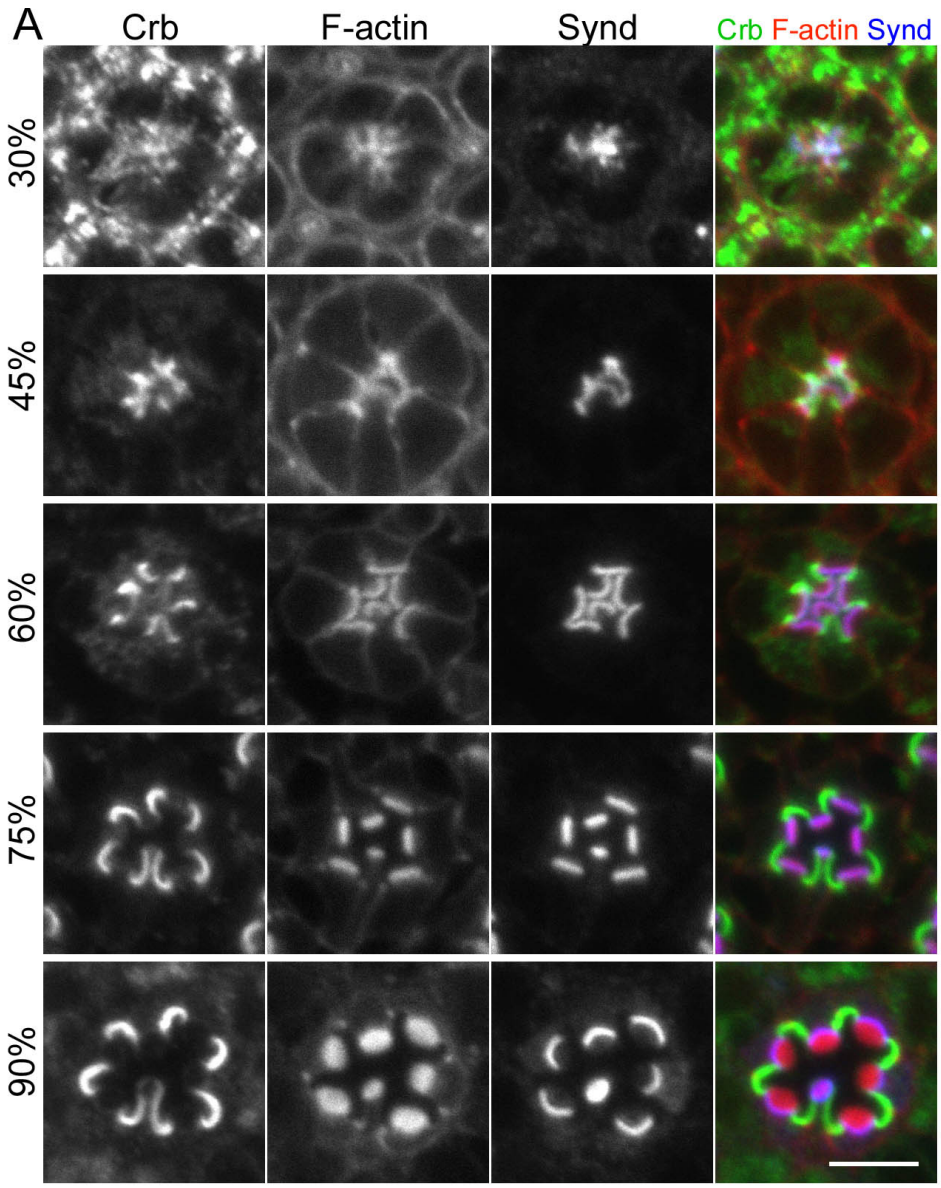

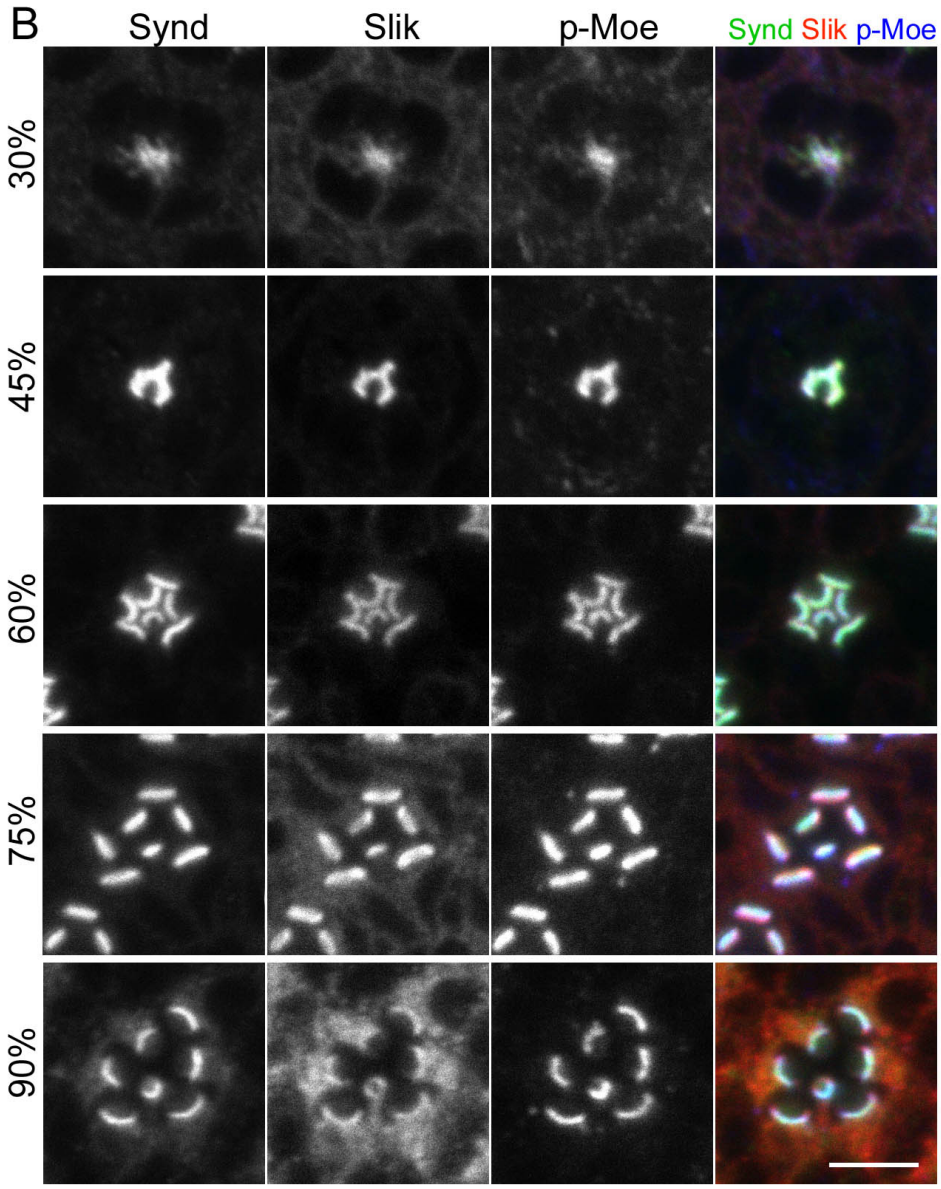

Fig. S4 Synd, Crb, p-Moe, and Slik localization in ommatidia during development. (A) Immunostaining of the w^{1118} (wild-type) retinas from the pupae at 30%, 45%, 60%, 75%, and 90% pd by anti-Crb (green), phalloidin (red), and anti-Synd antibodies (blue). 4, 4, 3, 4 and 4 independent eyes were observed in 30%, 45%, 60%, 75% and 90%, respectively. (B) Immunostaining of w^{1118} (wild-type) retinas from the pupae at 30%, 45%, 60%, 75%, and 90% pd by anti-Synd (green), Slik (red), and anti-p-Moe antibodies (blue). 7, 10, 4, 4 and 3 independent eyes were observed in 30%, 45%, 60%, 75% and 90%, respectively. Scale bar: 5 μm (A, B).

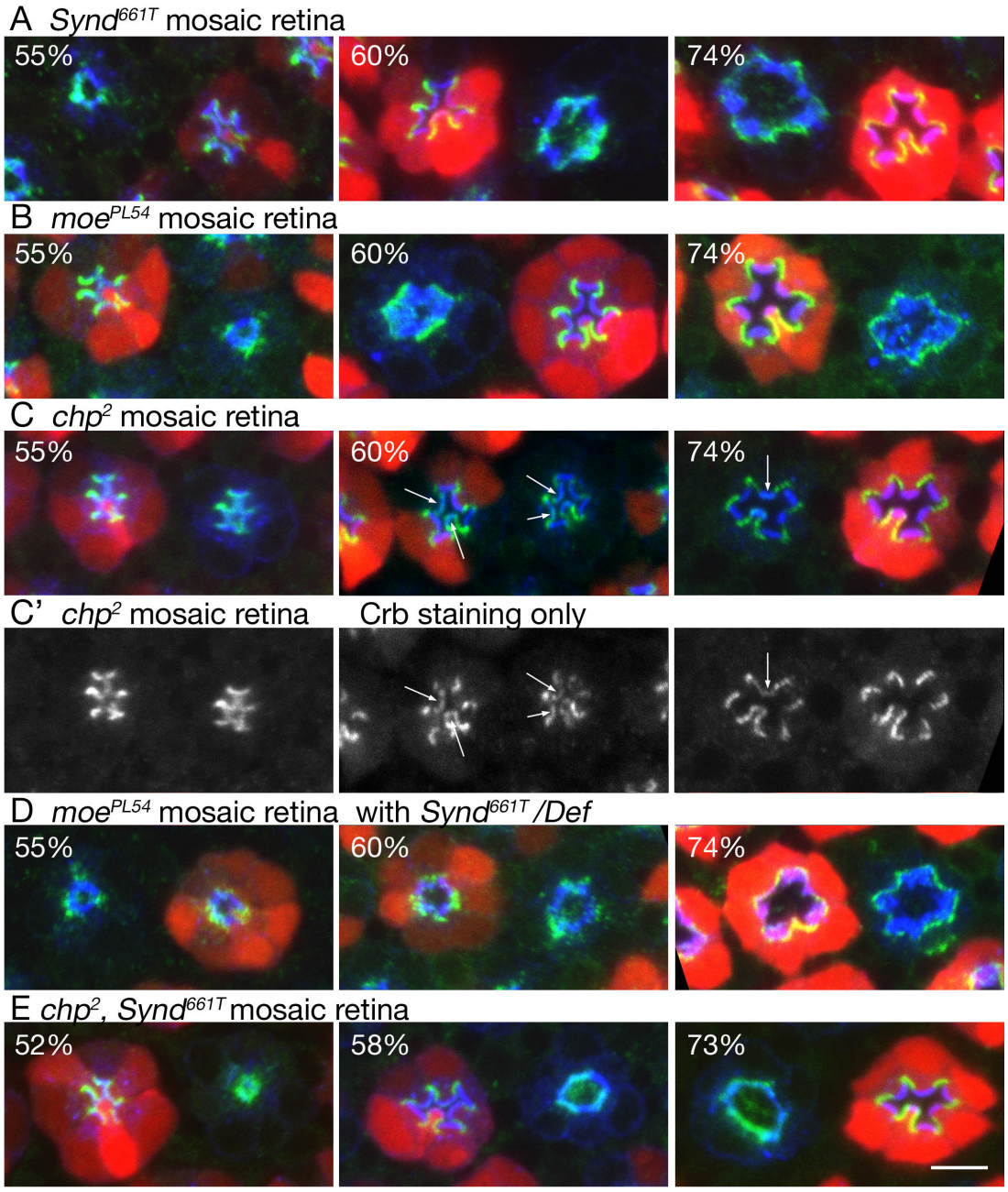

Fig. S5 Stalk-rhabdomere segregation in *Synd*^{661T}, *Moe*^{PL54}, and *chp*^{2} single and double mutant ommatidia during development. (A–D) Immunostaining of the mosaic retinas with indicated genotypes from the pupae at 55%, 60%, and 74% pd by anti-Crb (green) and anti-TRP antibodies (blue). RFP (red) indicates the wild-type (A–C) or *Synd*^{661T} single mutant photoreceptors (D). C' shows anti-TRP staining of *chp*^{2} mosaic retina (C). (E) Immunostaining of *chp*^{2} and *Synd*^{661T} double mutant mosaic retinas from the pupae at 52%, 58%, and 73% pd by anti-Crb (green) and anti-TRP antibodies (blue). RFP (red) indicates the wild-type. Scale bar: 5 μm (A–E).

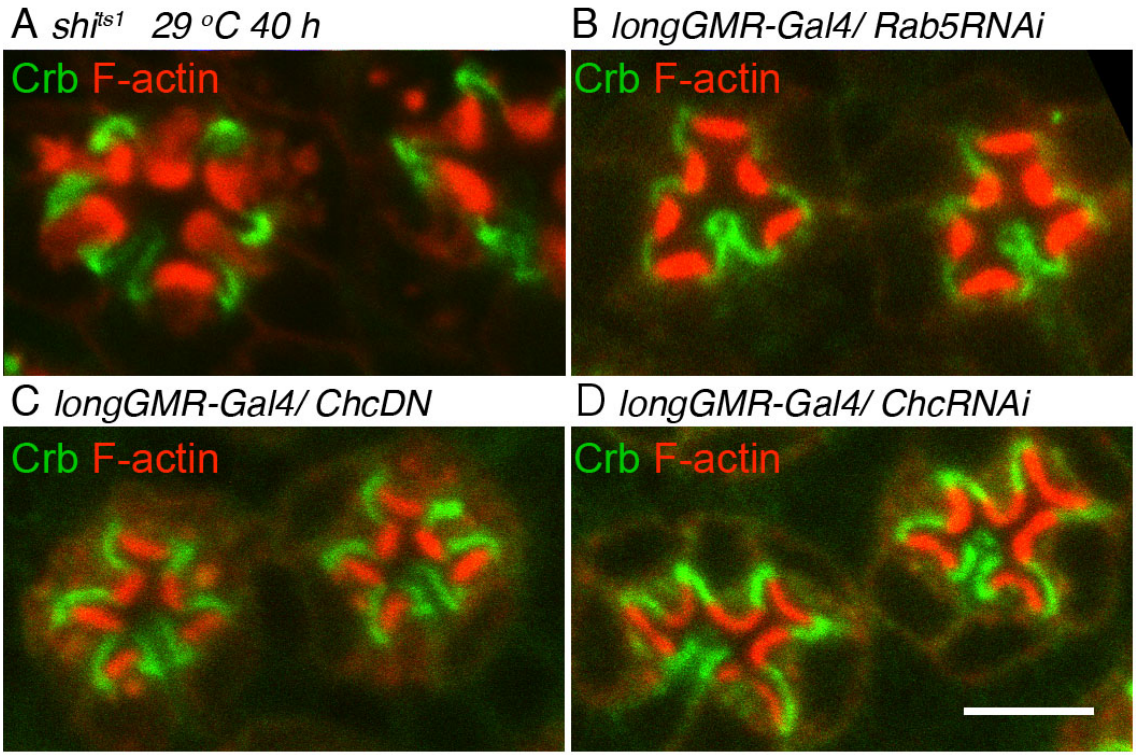

Fig. S6 Endocytosis is not required for stalk-rhabdomere segregation. (A-D) (A) Immunostaining of retinas from *shi*^{ts1} homozygous flies by anti-Crb antibody (green) and F-actin (red). *shi*^{ts1} homozygous flies are maintained at 20 °C, and unstaged pupae were randomly corrected and incubated at 29°C for 40 h, and pupae with gray-wings were fixed, which are supposed to be 80-100% pd. (B-D) Immunostaining of retinas expressing Rab5RNAi (B), ChcDN (C) or Chc RNAi (D) by longGMR-Gal4 by using anti-Crb antibody (green) and F-actin (red). 2, 3, 4 and 5 independent eyes were observed in G, H, I and J, respectively. Scale bar: 5 μm (A, B).